Decaying Kolmogorov turbulence in a model of superflow

C. Nore[a)]
Laboratoire de Physique Statistique de l'Ecole Normale Supérieure associé au CNRS et aux Universités Paris 6 et 7, 24 Rue Lhomond, 75231 Paris Cedex 05, France

M. Abid
Institute de Recherche sur les Phénomènes Hors Equilibre UMR CNRS et Université d'Aix-Marseille I, service 252, Centre St-Jérôme, 13397 Marseille Cedex 20, France

M. E. Brachet
Laboratoire de Physique Statistique de l'Ecole Normale Supérieure associé au CNRS et aux Universités Paris 6 et 7, 24 Rue Lhomond, 75231 Paris Cedex 05, France

(Received 27 December 1996; accepted 9 May 1997)

Superfluid turbulence is studied using numerical simulations of the nonlinear Schrödinger equation (NLSE), which is the correct equation of motion for superflows at low temperatures. This equation depends on two parameters: the sound velocity and the coherence length. It naturally contains nonsingular quantized vortex lines. The NLSE mass, momentum, and energy conservation relations are derived in hydrodynamic form. The total energy is decomposed into an incompressible kinetic part, and other parts that correspond to acoustic excitations. The corresponding energy spectra are defined and computed numerically in the case of the two-dimensional vortex solution. A preparation method, generating initial data reproducing the vorticity dynamics of any three-dimensional flow with Clebsch representation is given and is applied to the Taylor–Green (TG) vortex. The NLSE TG vortex is studied with resolutions up to 512^3. The energetics of the flow is found to be remarkably similar to that of the viscous TG vortex. The rate of the (irreversible) transfer of kinetic energy into other energy components is comparable, both in magnitude and time scale, to the energy dissipation of the viscous flow. This transfer rate depends weakly on the coherence length. At the moment of maximum energy dissipation, the energy spectrum follows a power law compatible with Kolmogorov's $-5/3$ value. Physical-space visualizations show that the vorticity dynamics of the superflow is similar to that of the viscous flow in which vortex reconnection events play a major role. It is argued that there may be some amount of universality of reconnection processes, because of topological constraints. Some preliminary support for this conjecture is given in the special case of secondary instabilities of round jets. The experimental implications of the close analogy between superfluid and viscous decaying turbulence are discussed. © *1997 American Institute of Physics.* [S1070-6631(97)00909-4]

I. INTRODUCTION

Superfluid flows are described mathematically by the Landau two-fluid model, in contrast to classical ideal or viscous fluids, which are described by the Euler or Navier–Stokes equations, respectively.[1] When the temperature is low enough for the normal fluid to be negligible (in practice below $T=1$ K for helium at normal pressure), Landau's model reduces to the Euler equation for an ideal fluid, which is irrotational except on singular vortex lines around which the circulation of the velocity is quantized. The quantum nature of velocity circulation appears, in this model, as a supplementary condition, compatible with the Euler equation.

When both normal fluid and superfluid vortices are present, their interaction, called ''mutual friction,'' must be taken into account. Such models, pioneered by Schwarz,[2] are necessary, for example, to study superfluid turbulence in the counterflow produced by a heat current.

At low temperatures, an alternative mathematical description of superflows is given by the nonlinear Schrödinger equation (NLSE), sometimes also called the Gross–Pitaevskii equation.[3,4] The NLSE is a partial differential equation (PDE) for a complex wave field related to the superflow's density and velocity by Madelung's transformation.[5] The superflow is irrotational, except near the nodal lines (also called topological defect lines) of the complex wave field. These lines are known to follow Eulerian dynamics.[6–8] They are nonsingular, in contrast to the singular vortex lines in Landau's model. These topological defects correspond to the quantum vortices of superfluid helium; they appear naturally—with the correct amount of velocity circulation—in this model. In this context, NLSE is the correct dynamical equation of motion for superfluids.[9] Recently, because of the current availability of high-speed computers allowing numerical simulations to be performed, there has been a surge of interest in studying the dynamical properties of NLSE.[10–14] NLSE has been shown to contain intricate dynamical mechanisms, such as vortex reconnection,[14] vortex nucleation,[10] and vortex–sound interaction.[15]

One of the open problems in superfluidity is to explain the critical velocity at which superfluidity breaks down. This problem is related to the onset of superfluid turbulence. A

[a)]Also at: Laboratoire d'Informatique pour la Mécanique et les Sciences de l'Ingénieur, BP 133 91403 Orsay, Cedex, France.

 1070-6631/97/9(9)/2644/26/$10.00

question which has long been open is the degree of analogy between superfluid and ordinary turbulence. Quoting from Feynman's review of 1955: ''The resistance to flow somewhat above initial velocity must be the analogue in superfluid helium of turbulence, and a close analogue at that.''[16] Note that, experimentally, one should distinguish between counterflow superfluid turbulence and towed grid superfluid turbulence.[17] Counterflow superfluid turbulence is produced by a heat current and is characterized by opposite mass fluxes of normal fluid and superfluid. It has thus no classical analog. In contrast, in towed grid superfluid turbulence, the normal and superfluid components of the flow have the same velocity. It is the analog of ordinary turbulence and can exist at very low temperatures. In the rest of this article, we refer to towed grid superfluid turbulence simply as ''superfluid turbulence.''

The basic goal of the present article is to qualify the degree of analogy between superfluid and ordinary turbulence by comparing numerical simulations of NLSE and existing numerical simulations of Navier–Stokes equations. The comparison is made using the Taylor–Green (TG) vortex, a three-dimensional vortical flow characterized by a viscous decaying turbulence that is well documented in the literature.[18] The TG vortex is a standard turbulent flow used in numerical computations[19–21] that is related to an experimentally studied swirling flow.[22–24] The relation between the experimental flow and the TG vortex is a similarity in overall geometry:[22] a shear layer between two counter–rotating eddies. The TG vortex, however, is periodic with free-slip boundaries while the experimental flow is contained inside a tank between two counter–rotating disks. The TG vortex is also a highly symmetric flow which permits economical computations (see Ref. 19 and Appendix 1).

The paper is organized as follows: Section II is devoted to the basic definitions and properties of the model of superflow. A short presentation of the hydrodynamic form, through Madelung's transformation, of NLSE with an arbitrary nonlinearity is given. Simple solutions are discussed. Most of this section can be skipped by the reader already familiar with the NLSE model of superflow who will find, at the end of the section, the nonlinearity used for the numerical simulations presented in this article.

In Sec. III, the basic tools that are needed to numerically study three-dimensional turbulence using NLSE are developed and validated. The conservation relations for mass, momentum, and energy are derived. Energy spectra are defined, and computed in the case of a simple vortex solution. A preparation method for the initial data is developed. Using this method, the vorticity dynamics of any three-dimensional incompressible flow that admits a Clebsch representation can be reproduced with NLSE. The method is validated on a two-dimensional vortical test flow. The energy spectra are computed, and it is shown that their low wave number behavior is controlled by the classical flow, while their high wave number behavior is controlled by the (constant) number of vortices.

In Sec. IV, a Clebsch representation is given for the Taylor–Green vortex, a reference flow in the numerical study of (viscous) three-dimensional turbulence. This representation is used to generate initial data for NLSE. The corresponding vortex dynamics is compared to high resolution simulations of the Taylor–Green flow published in the literature. Evidence for Kolmogorov turbulence in NLSE is found, and its validity and meaning are discussed. Section V is our conclusion. The numerical methods and computer codes are described in an appendix.

II. BASIC DEFINITIONS AND PROPERTIES OF THE MODEL

Most of the material contained in this section can be skipped by the reader already familiar with the NLSE model of superflow.[25,6–8,5,9] We present the hydrodynamic form of NLSE with an arbitrary nonlinearity. We show that NLSE corresponds, through Madelung's transformation, to a barotropic fluid with an arbitrary equation of state. We also discuss basic hydrodynamic features such as time-independent solutions and acoustic propagation. The equation of state and the model parameters used for the numerical simulations presented in this article are defined at the end of the section.

A. Fluid dynamical form of the nonlinear wave equation

The most straightforward way to understand the relation between nonlinear wave dynamics and fluid dynamics is to first define the nonlinear wave dynamics through the following action functional:[25]

$$\mathscr{A}=2\alpha\int dt\left\{\int d^3x\left[\frac{i}{2}\left(\overline{\psi}\frac{\partial\psi}{\partial t}-\psi\frac{\partial\overline{\psi}}{\partial t}\right)\right]-\mathscr{F}\right\} \tag{1}$$

with

$$\mathscr{F}=\int d^3x[\alpha|\,\boldsymbol{\nabla}\psi|^2+f(|\psi|^2)], \tag{2}$$

where $\psi(\mathbf{x},t)$ is a complex wave field and $\overline{\psi}$ its complex conjugate, α is a positive real constant, and f is a polynomial in $|\psi|^2\equiv\overline{\psi}\psi$ with real coefficients:

$$f(|\psi|^2)=-\Omega|\psi|^2+\frac{\beta}{2}|\psi|^4+f_3|\psi|^6+\cdots+f_n|\psi|^{2n}. \tag{3}$$

The nonlinear wave dynamics is governed by the NLSE which is the Euler–Lagrange equation of motion for ψ corresponding to (1):

$$\frac{\partial\psi}{\partial t}=-i\frac{\delta\mathscr{F}}{\delta\overline{\psi}},$$

or

$$\frac{\partial\psi}{\partial t}=i[\alpha\,\boldsymbol{\nabla}^2\psi-\psi f'(|\psi|^2)]. \tag{4}$$

The key step is Madelung's transformation[5,25]

$$\psi=\sqrt{\rho}\,\exp\left(i\frac{\phi}{2\alpha}\right), \tag{5}$$

which maps the nonlinear wave dynamics of ψ into equations of motion for a fluid of density ρ and velocity $\mathbf{v}=\boldsymbol{\nabla}\phi$. Indeed with the help of (5), (1) can be written

$$\mathscr{A}=-\int dt\ d^3x\left\{\rho\frac{\partial\phi}{\partial t}+\frac{1}{2}\rho(\boldsymbol{\nabla}\phi)^2+2\alpha f(\rho)+\frac{1}{2}[2\alpha\,\boldsymbol{\nabla}(\sqrt{\rho})]^2\right\} \tag{6}$$

and the corresponding Euler–Lagrange equations of motion read

$$\frac{\partial\rho}{\partial t}+\boldsymbol{\nabla}\cdot(\rho\mathbf{v})=0, \tag{7}$$

$$\frac{\partial\phi}{\partial t}+\frac{1}{2}(\boldsymbol{\nabla}\phi)^2+2\alpha f'(\rho)-2\alpha^2\frac{\boldsymbol{\Delta}\sqrt{\rho}}{\sqrt{\rho}}=0. \tag{8}$$

Neglecting the last term of (8) (the so-called ''quantum pressure'' term), these equations are the continuity and Bernoulli equations[1] for an isentropic, compressible, irrotational fluid. Note that the quantum pressure term contains higher order spatial derivatives than the other terms in (8). It will turn out (see Sec. II C) that there are circumstances in which it can safely be neglected.

Using this identification, one can define the corresponding ''thermodynamic functions'' for the barotropic fluid. The fluid is called barotropic because only one thermodynamic variable (e.g., the density ρ) is enough to define its state at rest. By inspection of (6), the fluid's internal energy *per unit mass* is given by

$$e=\frac{2\alpha f(\rho)}{\rho} \tag{9}$$

and Bernoulli's Eq. (8) readily gives the fluid's enthalpy *per unit mass* as

$$h=2\alpha f'(\rho). \tag{10}$$

The thermodynamic identity

$$h=e+p/\rho, \tag{11}$$

yields, for the fluid's pressure, the expression

$$p=2\alpha[\rho f'(\rho)-f(\rho)]. \tag{12}$$

The physical dimensions of the variables used in (2) and (3) are fixed by the following considerations. Madelung's transformation (5) imposes that $[|\psi|^2]=[\rho]=M\ L^{-3}$ and $[\alpha]=L^2\ T^{-1}$. Using (9), one gets $[f(\rho)/\rho]=T^{-1}$ and thus, from (3), $[\Omega]=T^{-1}$, $[\beta]=T^{-1}\ \rho^{-1}$ and $[f_i]=T^{-1}\ \rho^{1-i}$. In the case of a Bose condensate of particles of mass, m, α has the value $\hbar/2m$.[9]

B. Elementary solutions

In this section, the elementary solutions of NLSE are presented. These correspond to a condensate at rest or an axisymmetric two-dimensional vortex at rest. The acoustic excitations around such solutions are discussed.

1. Fluid at rest

Further insight into the relation between nonlinear wave and fluid dynamics can be obtained by considering stationary solutions of the equations of motion. Indeed, time-independent solutions of NLSE (4) are also trivially solutions of the Real Ginzburg—Landau equation (RGLE)

$$\frac{\partial\psi}{\partial t}=-\frac{\delta\mathscr{F}}{\delta\overline{\psi}}=[\alpha\,\boldsymbol{\nabla}^2\psi-\psi f'(|\psi|^2)]. \tag{13}$$

They are thus extrema of the energy functional $\mathscr{F}$.

The simplest solution of this type corresponds to a constant density fluid at rest. In this simple case, ψ is constant in space and (13) reads

$$f'(|\psi|^2)=-\Omega+\beta|\psi|^2+3f_3|\psi|^4+\cdots+nf_n|\psi|^{2n-2}=0. \tag{14}$$

This equation, for given values of the coefficients β and f_i $(i=3,\ldots,n)$, relates the fluid density $|\psi|^2$ to the value of Ω.

Note that the Ω term of f does not play a crucial role in the NLSE dynamics. Indeed, it corresponds to a constant in (14) that could be removed from the Bernoulli Eq. (8) by the change of variable $\phi\rightarrow\phi+2\alpha\Omega t$. This change of Bernoulli potential ϕ amounts to a change of phase $\psi\rightarrow\psi e^{i\Omega t}$ in NLSE (4). We will however, by convention, not perform these changes of variable, in order that stationary solutions of (13) coincide with stationary solutions of (4). The Ω term of f will thus be related to the density $|\psi|^2$ of the fluid at rest through Eq. (14).

2. Vortex solution

Another important type of time-independent solutions of NLSE are the vortex solutions. Madelung's transformation is singular when $\rho=0$ (i.e., when both the real and the imaginary parts of ψ are zero). As two conditions are required, the singularities generically happen on points in two dimensions and lines in three dimensions. The circulation of $\mathbf{v}$ around such a generic singularity is $\pm4\pi\alpha$. These topological defects are known in the context of superfluidity as ''quantum vortices.''[5] Solutions of (13) with cylindrical symmetry can be obtained numerically.[26] It can be shown that, as r goes to zero, $\rho\sim r^2$ and $\mathbf{v}=2\alpha\mathbf{e}_{\boldsymbol{\theta}}/r$ where $\mathbf{e}_\theta$ is the azimuthal unit vector and r the radial distance of a cylindrical coordinate system $(\mathbf{e}_r,\mathbf{e}_\theta,\mathbf{e}_x)$ having its origin on the vortex line. The density admits a horizontal tangent at the origin $r=0$ while the velocity diverges as the inverse of the distance. Then the momentum density $\rho\mathbf{v}$ is a regular quantity.

An important property of vortex solutions is that they are *regular solutions* of NLSE. The singularity lies only in Madelung's transformation (5). This means that, when vortices are present, the fluid dynamical form of the action (6) and the corresponding Euler–Lagrange equations of motion (7), (8) are not well defined. We shall come back to this subtle point in Sec. III A.

C. Acoustic regime

The nature of the extra quantum pressure term in (8) can be understood by computing the dispersion relation corresponding to acoustic waves propagating around a constant density level ρ_0. Setting $\rho=\rho_0+\delta\rho$ [with $f'(\rho_0)=0$], $\boldsymbol{\nabla}\phi=\delta u$ in (7) and in the gradient of (8), one gets at linear order $\partial_t{}^2\delta\rho=2\alpha\rho_0 f''(\rho_0)\boldsymbol{\Delta}\delta\rho-\alpha^2\boldsymbol{\Delta}^2\delta\rho$. The dispersion re-

lation for an acoustic wave $\delta\rho=\epsilon\{\exp[i(\omega t-\mathbf{k}\cdot\mathbf{x})]+\text{c.c.}\}$ (with $\epsilon\ll 1$) is thus $\omega=\sqrt{2\alpha\rho_0 f''(\rho_0)k^2+\alpha^2k^4}$. This relation shows that the quantum pressure has a dispersive effect that becomes important for large wave numbers. For small wave numbers, one recovers the usual propagation, with a sound velocity given by

$$c=\left(\frac{\partial p}{\partial\rho}\right)^{1/2}=\sqrt{2\alpha\rho_0 f''(\rho_0)}. \tag{15}$$

This means that, for small wave number acoustic waves, the last term of (8) does not play a significant role. The length scale

$$\xi=\sqrt{\alpha/[\rho_0 f''(\rho_0)]} \tag{16}$$

at which dispersion becomes noticeable is known as the ''coherence length.''

All numerical results presented in this paper are performed using the simplest choice of nonlinearity for NLSE corresponding to a compressible fluid, namely

$$f(\rho)=-\Omega\rho+\frac{\beta}{2}\rho^2. \tag{17}$$

This simplest choice corresponds to the following thermodynamic quantities:

$$e=\frac{2\alpha}{\rho}\left(-\Omega\rho+\frac{\beta}{2}\rho^2\right), \tag{18}$$

$$h=2\alpha(-\Omega+\beta\rho), \tag{19}$$

$$p=\alpha\beta\rho^2. \tag{20}$$

The form of f used in our numerical computations (17), together with (15) and (16), lead to the following relations:

$$\begin{aligned} c&=\sqrt{2\alpha\beta},\\ \xi&=\sqrt{\alpha/\Omega},\\ \rho_0&=\Omega/\beta. \end{aligned} \tag{21}$$

When performing numerical computations, we will further fix the density to $\rho_0=1$. The coefficients of (17) used in the computations are thus defined in terms of c and ξ by the relations:

$$\begin{aligned} \alpha&=c\xi/\sqrt{2},\\ \beta&=c/(\sqrt{2}\xi),\\ \Omega&=\beta. \end{aligned} \tag{22}$$

III. CONSERVED QUANTITIES, INITIAL DATA PREPARATION, AND VALIDATIONS

This section is devoted to the development and validation of the basic tools that are needed to numerically study three-dimensional turbulence using NLSE.

We will redefine Madelung's transformation when vortex lines are present; this is necessary because the original transformation (5) is singular on vortex lines. This enables us to derive mass, momentum, and energy conservation relations, both in wave and hydrodynamic variables. These conservation laws are shown to be globally regular on vortices, and lead to the usual form for the fluid's equation of motion.

We use the expression for the total energy density in physical space and Parseval's formula to define energy spectra; these allow us to separate the various contributions to the total energy. The energy spectra are computed for the two-dimensional time-independent vortex solution.

We then describe a method for preparing initial data. This method allows us to generate initial data for NLSE that will reproduce the vorticity dynamics, without too much sound wave emission, of any given three-dimensional incompressible flow field, provided that this field admits a Clebsch representation.

The preparation method is validated on a two-dimensional vortical test flow. The vortex dynamics reproduces that of the classical incompressible flow, without too much sound emission. The energy spectra are computed; their low wave number behavior is consistent with that of the classical flow, while their high wave number behavior is controlled by the (constant) number of vortices.

A. Conserved quantities and Madelung's transformation

As stated in Sec. II B 2 and by using Madelung's transformation (5), a vortex line is given by $\psi=\sqrt{\rho}\exp(i\phi/2\alpha)=0$. Thus, on a vortex line, ϕ is not determined and so the equations of motions (7) and (8) are not well defined. This is a mathematical pathology of the transformation, without any physical meaning. To avoid this problem, we use Noether's theorem[27] to derive equations of motion well defined on a vortex line.

The invariance of (1) with respect to phase rotation, space translation, and time translation, respectively, yield the following conservation laws for mass, momentum, and energy (using the Einstein convention on repeated indices):

$$\partial_t(\psi\overline{\psi})+\partial_k[i\alpha(\psi\partial_k\overline{\psi}-\overline{\psi\partial_k\psi})]=0, \tag{23}$$

$$\begin{aligned} &\partial_t[i\alpha(\psi\partial_j\overline{\psi}-\overline{\psi\partial_j\psi})]+\partial_k[2\alpha^2(\partial_k\overline{\psi\partial_j\psi}+\partial_k\psi\partial_j\overline{\psi})\\ &\quad+(2\alpha|\psi|^2f'(|\psi|^2)-2\alpha f(|\psi|^2)-\alpha^2\partial_{ll}|\psi|^2)\delta^k_j]=0, \end{aligned} \tag{24}$$

$$\begin{aligned} &\partial_t[2\alpha^2\partial_k\psi\partial_k\overline{\psi}+2\alpha f(|\psi|^2)]-2\alpha^2\partial_k[i\alpha(\partial_k\overline{\psi\partial_{jj}\psi}\\ &\quad-\partial_k\psi\partial_{jj}\overline{\psi})+if'(|\psi|^2)(\overline{\psi\partial_k\psi}-\psi\partial_k\overline{\psi})]=0. \end{aligned} \tag{25}$$

Using Madelung's transformation (5) in the form:

$$\begin{aligned} \rho&=|\psi|^2,\\ \rho v_j&=i\alpha(\psi\partial_j\overline{\psi}-\overline{\psi\partial_j\psi}), \end{aligned} \tag{26}$$

and with the thermodynamic definitions of the internal energy, e (9), enthalpy, h (10), and pressure, p (12), the conservation laws, after some algebra, can be cast in the form:

$$\frac{\partial\rho}{\partial t}+\partial_i(\rho v_i)=0, \tag{27}$$

$$\frac{\partial\rho v_j}{\partial t}+\partial_i\left[\rho v_i v_j+4\alpha^2\partial_i\sqrt{\rho}\partial_j\sqrt{\rho}+(p-\alpha^2\partial_{kk}\rho)\delta^i_j\right]=0, \tag{28}$$

$$\frac{\partial}{\partial t}\left[2\alpha^2(\partial_j\sqrt{\rho})^2+\frac{1}{2}\rho v_j v_j+\rho e\right]$$
$$=-\partial_i\left(\rho v_i h+\frac{1}{2}\rho v_i v_j v_j\right)-\partial_i\left[\alpha^2\frac{\partial_i\rho}{\rho}\partial_j(\rho v_j)\right.$$
$$\left.-2\alpha^2\sqrt{\rho}v_i\partial_{jj}\sqrt{\rho}\right]. \tag{29}$$

These conservation laws, apart from the extra quantum pressure terms (recognizable by the α^2 factor), are the standard conservation laws[1] for a classical barotropic fluid.

Let us now show that (27)–(29) are nonsingular, even for vortex solutions. In fact, as r goes to zero, $\rho\sim r^2$ and $\mathbf{v}=2\alpha\mathbf{e}_\theta/r$, where $\mathbf{e}_\theta$ is the azimuthal unit vector and r the radial distance of a cylindric coordinate system $(\mathbf{e}_r,\mathbf{e}_\theta,\mathbf{e}_x)$ having its origin on a vortex line. Thus, in Eq. (28), the term $\rho\mathbf{v}\otimes\mathbf{v}\sim 4\alpha^2\mathbf{e}_\theta\otimes\mathbf{e}_\theta$ ($\otimes$ is the tensor product) is not defined at $r=0$. The same thing happens for $4\alpha^2\boldsymbol{\nabla}\sqrt{\rho}\otimes\boldsymbol{\nabla}\sqrt{\rho}\sim 4\alpha^2\mathbf{e}_r\otimes\mathbf{e}_r$ but the sum of these two terms is independent of θ and therefore is well defined at the origin. Since the remaining terms are all regular at a vortex line, Eq. (28) is regular. In Eq. (29), as r goes to zero, $\rho\mathbf{v}v^2\sim 4\alpha^2\mathbf{e}_\theta/r$. This singularity cancels with that of $-2\alpha^2\sqrt{\rho}\mathbf{v}\boldsymbol{\Delta}\sqrt{\rho}\sim -4\alpha^2\mathbf{e}_\theta/r$. The other terms are regular.

In order to derive equations of motion similar to (7) and (8) and well defined on a vortex line, we use (27) and (28) to obtain

$$\rho\frac{\partial v_j}{\partial t}-v_j\partial_i(\rho v_i)+\partial_i\left[\rho v_i v_j+4\alpha^2\partial_i\sqrt{\rho}\partial_j\sqrt{\rho}+(p\right.$$
$$\left.-\alpha^2\partial_{kk}\rho)\,\delta^i_j\right]=0, \tag{30}$$

which leads to

$$\rho\left(\frac{\partial v_j}{\partial t}+v_i\partial_i v_j\right)=-\partial_j(p-\alpha^2\partial_{kk}\rho)$$
$$-\partial_i(4\alpha^2\partial_i\sqrt{\rho}\partial_j\sqrt{\rho}). \tag{31}$$

As r goes to zero, all the terms but $\rho(\mathbf{v}\cdot\boldsymbol{\nabla})\mathbf{v}\sim -4\alpha^2\mathbf{e}_r/r$ and $\boldsymbol{\nabla}\cdot(4\alpha^2\boldsymbol{\nabla}\sqrt{\rho}\otimes\boldsymbol{\nabla}\sqrt{\rho})\sim 4\alpha^2\mathbf{e}_r/r$ are regular. Just as for the Eq. (28), these singularities cancel on a vortex line. To recognize the Bernoulli Eq. (8), we need to rewrite the right-hand side of (31). Using Eq. (12) for p and writing $\partial_{kk}\rho=\partial_{kk}(\sqrt{\rho})^2=2\sqrt{\rho}\partial_{kk}\sqrt{\rho}+2(\partial_k\sqrt{\rho})^2$, one can find that the right-hand side of Eq. (31) is equal to $-\rho\partial_j(h-2\alpha^2\boldsymbol{\Delta}\sqrt{\rho}/\sqrt{\rho})$, and thus Eq. (31) reads

$$\rho\left(\frac{\partial v_j}{\partial t}+v_i\partial_i v_j\right)=-\rho\partial_j\left(h-2\alpha^2\frac{\boldsymbol{\Delta}\sqrt{\rho}}{\sqrt{\rho}}\right), \tag{32}$$

which is the gradient of Eq. (8) multiplied by ρ for an irrotational fluid. This equation is the standard Euler equation for a barotropic fluid, apart from the quantum pressure term, $2\alpha^2\boldsymbol{\Delta}\sqrt{\rho}/\sqrt{\rho}$.

B. Energy spectra

In this section, we will use the conserved energy density derived in Sec. III A and Parseval's identity to define energy spectra. The spectra corresponding to the two-dimensional time independent vortex solution are calculated.

1. Definitions of the energy spectra

Starting from the energy conservation law (29), the total energy $E_{\rm tot}$ can naturally be decomposed into the kinetic, internal, and ''quantum'' energies:

$$E_{\rm tot}=E_{\rm kin}+E_{\rm int}+E_q. \tag{33}$$

Using (9) and (29), each of these parts can be formally defined as the (space) integral of the square of a field:

$$E_{\rm kin}=\frac{1}{2(2\pi)^3}\int d^3x(\sqrt{\rho}v_j)^2, \tag{34}$$

$$E_{\rm int}=\frac{1}{2(2\pi)^3}\int d^3x\left[2\sqrt{\alpha f(\rho)}\right]^2, \tag{35}$$

$$E_q=\frac{1}{2(2\pi)^3}\int d^3x(2\alpha\partial_j\sqrt{\rho})^2. \tag{36}$$

These denominations are justified by the expression in terms of ρ and v of $E_{\rm kin}$, by expression (9) for the fluid's internal energy and by the correspondence between E_q and the quantum pressure term in (31).

Because of energy conservation (29), $E_{\rm tot}$ will remain constant during evolution under NLSE dynamics. However, each of the individual energy components $E_{\rm kin}$, $E_{\rm int}$, and E_q can, and, in general, will vary in time. Thus, by monitoring their values, some understanding of the energy transfers in the system can be achieved. Such an understanding can be enhanced by a scale-by-scale energy breakdown for each individual component. Each component being the space integral of a squared field, Parseval's theorem allows us to construct energy spectra. Indeed, defining the normalization of the Fourier transform as $g(\mathbf{r})=\int d^3k e^{-ik_jr_j}\hat{g}(\mathbf{k})$, one gets $\hat{g}(\mathbf{k})=(2\pi)^{-3}\int d^3r e^{ik_jr_j}g(\mathbf{r})$, and Parseval's theorem reads $\int d^3k|\hat{g}(\mathbf{k})|^2=(2\pi)^{-3}\int d^3r|g(\mathbf{r})|^2$. Thus, by computing the Fourier transform of $\sqrt{\rho}v_j$, $2\sqrt{\alpha f(\rho)}$, and $2\alpha\partial_j\sqrt{\rho}$, respectively, and integrating their square modulus over the angles, one gets the following energy spectra:

$$E_{\rm kin}(k)=\frac{1}{2}\int d\Omega_k\left|\frac{1}{(2\pi)^3}\int d^3r e^{ir_nk_n}\sqrt{\rho}v_j\right|^2,$$
$$E_{\rm int}(k)=\frac{1}{2}\int d\Omega_k\left|\frac{1}{(2\pi)^3}\int d^3r e^{ir_nk_n}2\sqrt{\alpha f(\rho)}\right|^2, \tag{37}$$
$$E_q(k)=\frac{1}{2}\int d\Omega_k\left|\frac{1}{(2\pi)^3}\int d^3r e^{ir_nk_n}2\alpha\partial_j\sqrt{\rho}\right|^2,$$

where $d\Omega_k$ denotes $k^2\sin\theta\,d\theta\,d\varphi$ in spherical coordinates. They verify by construction the relations $E_{\rm kin}=\int_0^\infty dkE_{\rm kin}(k)$, $E_{\rm int}=\int_0^\infty dkE_{\rm int}(k)$, and $E_q=\int_0^\infty dkE_q(k)$. Furthermore, in order to separate the kinetic energy corresponding to compressibility effects, we decompose $\sqrt{\rho}v_j$ in $\sqrt{\rho}v_j=(\sqrt{\rho}v_j)^i+(\sqrt{\rho}v_j)^c$ with $\boldsymbol{\nabla}\cdot(\sqrt{\rho}v_j)^i=0$. The corre-

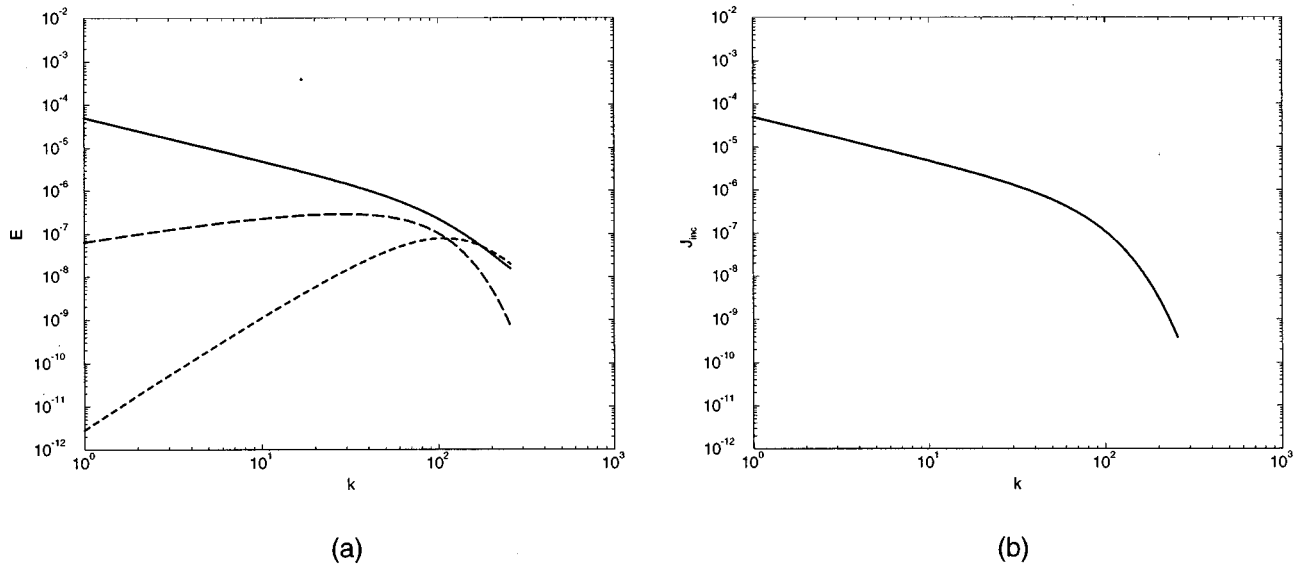

FIG. 1. Plots of the energy spectra (a) and momentum density spectrum (b) corresponding to an axisymmetric two-dimensional vortex. The spectra are computed from (41) and (42) with 18 Chebychev polynomials and with coherence length $\xi=0.1/(8\sqrt{2})$, and sound velocity $c=2$. Fig. 1 (a) shows the kinetic energy $E_{\rm kin}$ (solid), the quantum energy E_q (dashed) and the internal energy $E_{\rm int}$ (long–dashed).

sponding spectra are named $E^i_{\rm kin}(k)$ and $E^c_{\rm kin}(k)$, satisfying the relation $E_{\rm kin}(k)=E^i_{\rm kin}(k)+E^c_{\rm kin}(k)$. We also compute the spectrum associated with ρv_j, i.e.,

$$J(k)=\frac{1}{2}\int d\Omega_k\left|\frac{1}{(2\pi)^3}\int d^3re^{ir_nk_n}\rho v_j\right|^2, \tag{38}$$

called the momentum density spectrum.

The precise way in which the angle average is performed in the case of periodic fields is explained in Appendix 3.

We will also wish to compute spectra in the (r,θ) plane. The appropriate definitions of the two-dimensional energy spectra and momentum density spectrum are

$$E_{\rm kin}(k)=\frac{1}{2}\int_0^{2\pi}kd\theta\left|\frac{1}{(2\pi)^2}\int d^2re^{ir_nk_n}\sqrt{\rho}v_j\right|^2 \tag{39a}$$

$$E_{\rm int}(k)=\frac{1}{2}\int_0^{2\pi}kd\theta\left|\frac{1}{(2\pi)^2}\int d^2re^{ir_nk_n}2\sqrt{\alpha f(\rho)}\right|^2, \tag{39b}$$

$$E_q(k)=\frac{1}{2}\int_0^{2\pi}kd\theta\left|\frac{1}{(2\pi)^2}\int d^2re^{ir_nk_n}2\alpha\partial_j\sqrt{\rho}\right|^2, \tag{39c}$$

and

$$J(k)=\frac{1}{2}\int_0^{2\pi}kd\theta\left|\frac{1}{(2\pi)^2}\int d^2re^{ir_nk_n}\rho v_j\right|^2. \tag{40}$$

2. The energy spectra of a two-dimensional vortex

For an axisymmetric two-dimensional vortex, the divergence of $\sqrt{\rho}v_j$ and of ρv_j are zero. Thus the compressible parts of the corresponding spectra vanish.

Each of the spectra (39) and (40) is related to the two-dimensional Fourier transform of an isotropic function: $E_{\rm kin}(k)$ to the curl of $2\alpha\sqrt{\rho}\mathbf{e}_\theta/r$, $E_{\rm int}(k)$ to the function $2\sqrt{\alpha f(\rho)}$, $E_q(k)$ to the gradient of $2\alpha\sqrt{\rho}$, and $J(k)$ to the curl of $2\alpha\rho\mathbf{e}_\theta/r$. Using the expression of the Fourier transform appropriate to an isotropic function $g(r)$, $\hat{g}(k)=(2\pi)^{-1}\int_0^\infty drrJ_0(kr)g(r)$, where J_0 is the zero order Bessel function, we can express the energy spectra (39) as

$$E_{\rm kin}(k)=\frac{1}{4\pi k}\left[\int_0^\infty drrJ_0(kr)\frac{2\alpha}{r}\frac{\partial\sqrt{\rho}}{\partial r}\right]^2,$$

$$E_{\rm int}(k)=\frac{k}{2\pi}\left[\int_0^\infty drrJ_0(kr)2\sqrt{\alpha f(\rho)}\right]^2, \tag{41}$$

$$E_q(k)=\frac{k^3}{4\pi}\left[\int_0^\infty drrJ_0(kr)2\alpha\sqrt{\rho}\right]^2,$$

and the momentum density spectrum (40) as

$$J(k)=\frac{1}{4\pi k}\left[\int_0^\infty drrJ_0(kr)\frac{4\alpha\sqrt{\rho}}{r}\frac{\partial\sqrt{\rho}}{\partial r}\right]^2. \tag{42}$$

Appendix 3 contains a description of the numerical method used to compute the integrals (41) and (42). The energy and momentum density spectra computed with this procedure are displayed in Fig. 1 with $\xi=0.1/(8\sqrt{2})$ and $c=2$.

Each of the spectra displays a change of behavior around the wave number $k_\xi\sim1/\xi=113$. The spectra $J(k)$ and $E_{\rm int}(k)$ show exponential decay for $k\gg k_\xi$. This is related to the absence of singularity of the integrands of (40) and (39b) near $r=0$. Indeed, it is well known that the Fourier transform of a function that is analytic in a finite strip decays exponentially at large wave numbers.[28] $E_{\rm kin}(k)$ and $E_q(k)$ have a power-law behavior for $k\gg k_\xi$ that reflects their singularity in $r=0$. Indeed, the Fourier transform of $g(r)\sim r^s$ (with s a positive real) is $\hat{g}(k)\sim k^{-s-2}$. Thus the associated angle averaged spectrum has a power-law behavior as

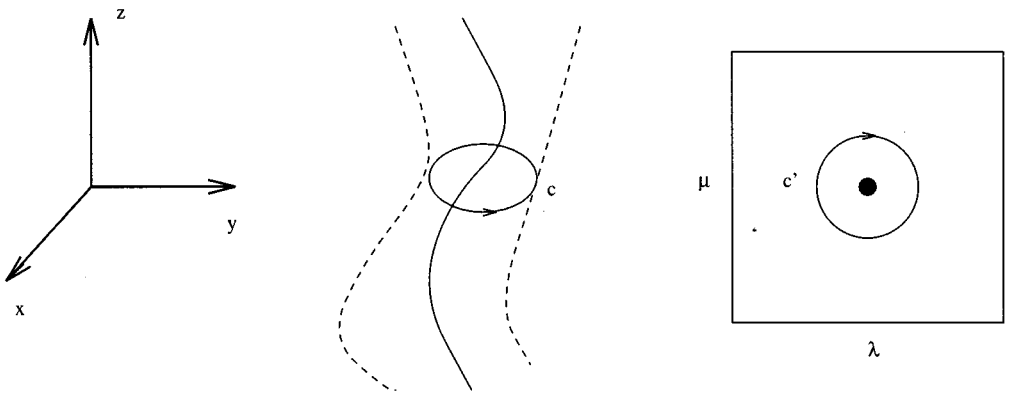

FIG. 2. A schematic representation of relations (44) and (47). The Clebsch potentials $\lambda(x,y,z),\mu(x,y,z)$ map the left-hand side of the figure into the (λ,μ) plane shown in the right-hand side. The circulation of $\mathbf{u}^{\mathrm{adv}}$ around the contour in physical space $\mathscr{C}$ is equal to the area inside the corresponding curve in the (λ,μ) plane $\mathscr{C}'$.

k^{-2s-3}. The small r behavior of both the integrands of (39a) and (39c) is r^0. This argument explains the k^{-3} power-law behavior at large k of $E_{\mathrm{kin}}(k)$ and $E_q(k)$ in Fig. 1(a).

The above Fourier transform scaling argument can be used to relate the $k \ll k_\xi$ power-law behavior of the spectra in Fig. 1 to the large r behavior of the corresponding integrands. Both ρv_j and $\sqrt{\rho} v_j$ behave as r^{-1} at large r, which gives a k^{-1} scaling for $k \ll k_\xi$. The k^3 small k scaling of $E_q(k)$ corresponds to the r^{-3} large r scaling of $\partial_j \sqrt{\rho}$. Finally, the k^1 small k scaling of $E_{\mathrm{int}}(k)$ is related to the r^{-2} large r scaling of $(\rho-1)$.

C. Initial data preparation method for vortical flows

Given a large scale flow $\mathbf{u}^{\mathrm{adv}}$ that admits a global Clebsch representation,[29] the initial data preparation method developed in this section will generate a vortex array whose NLSE dynamics will mimic the large scale flow vortex dynamics. The preparation method consists of two steps. In the first step, the Clebsch representation of $\mathbf{u}^{\mathrm{adv}}$ is used to construct a wave field $\psi(x,y,z)$ whose nodal lines are vortex lines of $\mathbf{u}^{\mathrm{adv}}$. In this way, one can generate a field with the distribution of nodal lines that reproduces the global circulation of $\mathbf{u}^{\mathrm{adv}}$. A second preparation step is needed in order to minimize the emission of acoustic waves. Indeed, starting a NLSE integration from an arbitrary initial data would generically lead to a transient emission of acoustic waves. Note that this is a general property of compressible flows.

1. Vortex arrays defined by global Clebsch variables

We consider a large scale flow $\mathbf{u}^{\mathrm{adv}}$ that admits a global Clebsch representation[29] in terms of two potentials:

$$\lambda = \lambda(x,y,z), \qquad \mu = \mu(x,y,z), \tag{43}$$

and of a function $V(x,y,z)$ such that:

$$\mathbf{u}^{\mathrm{adv}} = \lambda \boldsymbol{\nabla} \mu - \boldsymbol{\nabla} V, \tag{44}$$

with $\boldsymbol{\nabla}\cdot\mathbf{u}^{\mathrm{adv}}=0$. The vorticity $\boldsymbol{\omega}=\boldsymbol{\nabla}\times\mathbf{u}^{\mathrm{adv}}$ can thus be written

$$\boldsymbol{\omega} = \boldsymbol{\nabla}\lambda \times \boldsymbol{\nabla}\mu. \tag{45}$$

The circulation Γ of $\mathbf{u}^{\mathrm{adv}}$ around any contour $\mathscr{C}$ (see Fig. 2) can be written

$$\Gamma = \oint_{\mathscr{C}} \mathbf{u}^{\mathrm{adv}} \cdot d\mathbf{l} = \oint_{\mathscr{C}} \lambda \boldsymbol{\nabla}\mu \cdot d\mathbf{l} = \oint_{\mathscr{C}'} \lambda \, d\mu, \tag{46}$$

where $\mathscr{C}'$ is the circuit in the (λ,μ) plane corresponding to the circuit $\mathscr{C}$ in physical space (see Fig. 2). Using Stokes' formula, this integral can be written in the (λ,μ) plane as

$$\Gamma = \int\int_{S'} d\lambda \wedge d\mu, \tag{47}$$

where $\wedge$ is the outer product and S' is the surface enclosed by the circuit $\mathscr{C}'$. Note that, when a global Clebsch representation (43) exists, the dynamical system $dM/ds = \boldsymbol{\omega}[M(s)]$ admits λ,μ as first integrals such that $\lambda[M(s)]=\text{const}$, $\mu[M(s)]=\text{const}$. As a generic three-dimensional divergence-less vector field is nonintegrable,[30] a global Clebsch representation does not generically exist.

Equations (44) and (47) admit a simple geometrical representation in terms of vortex lines and velocity circulation. A vortex line in physical space is mapped into a point in the (λ,μ) plane. A circuit $\mathscr{C}$ defining a vortex tube in physical space is mapped into a contour $\mathscr{C}'$ in the (λ,μ) plane. The circulation of $\mathbf{u}^{\mathrm{adv}}$ around $\mathscr{C}$ corresponds to the surface inside $\mathscr{C}'$ in the (λ,μ) plane. This representation can be used to construct a complex three-dimensional field with a defect line corresponding to a vortex line of $\mathbf{u}^{\mathrm{adv}}$. Indeed, defining the three-dimensional field as

$$\psi(x,y,z) = \tilde{\psi}[\lambda(x,y,z),\mu(x,y,z)], \tag{48}$$

where $\tilde{\psi}(\lambda,\mu)$ is a complex two-dimensional field with a simple zero at $\lambda=\lambda_d$, $\mu=\mu_d$, the three-dimensional field ψ has, by construction, a nodal line along the vortex line of $\mathbf{u}^{\mathrm{adv}}$ defined by $\lambda(x,y,z)=\lambda_d, \mu(x,y,z)=\mu_d$. Furthermore, if $\tilde{\psi}$ has several simple zeroes, then the corresponding three-dimensional field ψ of (48) will have several nodal lines.

In practice, the number of zeroes of $\tilde{\psi}$ is fixed by the ratio of the total surface spanned on the (λ,μ) plane by the defining Clebsch potentials (43) to the quantum of circulation, $4\pi\alpha$, i.e.,

$$n_d=\left[\frac{\Gamma}{4\pi\alpha}\right], \tag{49}$$

where [ ] denotes the integer part of a real. See Secs. III D 1 and IV A for a practical implementation of this procedure.

2. Minimization of the modified energy functional

Under compressible fluid dynamics, the vortex array obtained using Clebsch potentials will generally lead to a regime containing a great deal of acoustic radiation. In order to study vortex dynamics using NLSE, we thus need to prepare the initial data in such a way that the acoustic emission is as small as possible. We know that the RGLE (13) with an initial data containing a nodal line converges towards the exact time-independent vortex solution ψ_v described in Sec. II B 2.

The procedure we have developed is a generalization of this property of RGLE. Our aim is to prepare an arbitrary assembly of moving vortices. To do so, we use the Galilean invariance of NLSE:

$$\psi(\mathbf{x},t)\rightarrow\psi(\mathbf{x}-\mathbf{u}^{\mathrm{adv}}t,t)\ \exp\left\{i\left[\frac{\mathbf{u}^{\mathrm{adv}}}{2\alpha}\cdot\mathbf{x}-\frac{(\mathbf{u}^{\mathrm{adv}})^2}{4\alpha}t\right]\right\},$$

for any constant boost velocity $\mathbf{u}^{\mathrm{adv}}$. This transformation maps any NLSE solution $\psi(\mathbf{x},t)$ into another NLSE solution whose associated velocity and density fields are Galilean transforms of those associated with ψ. Thus, the NLSE initial condition $\psi_v(\mathbf{x})\exp(i\mathbf{u}^{\mathrm{adv}}/2\alpha\cdot\mathbf{x})$ corresponds to a vortex translating with velocity $\mathbf{u}^{\mathrm{adv}}$. This initial condition can be directly obtained as a time-asymptotic solution of the advective real Ginzburg–Landau equation (ARGLE)

$$\frac{\partial\psi}{\partial t}=\alpha\boldsymbol{\nabla}^2\psi-\psi f'(|\psi|^2)-i\mathbf{u}^{\mathrm{adv}}\cdot\boldsymbol{\nabla}\psi-\frac{(\mathbf{u}^{\mathrm{adv}})^2}{4\alpha}\psi \tag{50}$$

and as a minimum of the associated modified energy functional

$$\mathscr{F}_{\mathrm{ARGLE}}[\psi,\overline{\psi}]=\int d^3\mathbf{x}\left(\alpha\left|\boldsymbol{\nabla}\psi-i\frac{\mathbf{u}^{\mathrm{adv}}}{2\alpha}\psi\right|^2+f(|\psi|^2)\right). \tag{51}$$

Our preparation method consists of using (50) and (51) with a given *space-dependent* divergence-free velocity field $\mathbf{u}^{\mathrm{adv}}(\mathbf{x})$. Using the Madelung transformation (26), (51) reads

$$\mathscr{F}_{\mathrm{ARGLE}}[\rho,\mathbf{v}]=\frac{1}{2\alpha}\int d^3\mathbf{x}\left\{\frac{1}{2}(2\alpha\boldsymbol{\nabla}\sqrt{\rho})^2+2\alpha f(\rho)+\frac{1}{2}\rho[\mathbf{v}-\mathbf{u}^{\mathrm{adv}}(\mathbf{x})]^2\right\}.$$

The last term on the right-hand side will be minimized if the velocity $\mathbf{v}$ is as close as possible to the imposed advective velocity $\mathbf{u}^{\mathrm{adv}}(\mathbf{x})$.

D. Validations on a two-dimensional vortical test flow

In this section, we introduce a simple two-dimensional test flow: a system of four counter-rotating vortices. This flow is a time-independent solution of the incompressible two-dimensional Euler equation. The trivial Eulerian dynamics of the test flow allows us to perform a global test of the preparation method introduced above. Furthermore, we develop and test a vortex counting procedure that will be used in the three-dimensional TG flow to measure the vortex line density.

1. Vortex array for the two-dimensional test flow

The two-dimensional vortical test flow is given by

$$\begin{aligned}u_x^{\mathrm{adv}}(x,y)&=\sin(x)\cos(y),\\ u_y^{\mathrm{adv}}(x,y)&=-\cos(x)\sin(y).\end{aligned} \tag{52}$$

The Clebsch potentials,

$$\begin{aligned}\lambda(x,y)&=\sqrt{2}\cos(x),\\ \mu(x,y)&=\sqrt{2}\cos(y),\end{aligned} \tag{53}$$

correspond to the flow (52) in the sense that $\boldsymbol{\nabla}\times\mathbf{u}^{\mathrm{adv}}=\boldsymbol{\nabla}\lambda\times\boldsymbol{\nabla}\mu=2\sin x\sin y\hat{\mathbf{z}}$. λ and μ are chosen to be periodic functions of (x,y) in order to permit computations in a periodic box.

The mapping between the (x,y) plane and the (λ,μ) plane is displayed in Fig. 3.

The two-dimensional complex field ψ_e with a simple zero at the origin of the (λ,μ) plane reads

$$\psi_e(\lambda,\mu)=(\lambda+i\mu)\frac{\tanh(\sqrt{\lambda^2+\mu^2}/\sqrt{2}\xi)}{\sqrt{\lambda^2+\mu^2}}, \tag{54}$$

where ξ is defined by Eq. (21).

The system of four zeroes in the (λ,μ) plane displayed in Fig. 3 corresponds to the product

$$\psi_4(\lambda,\mu)=\psi_e\left(\lambda-\frac{1}{\sqrt{2}},\mu\right)\psi_e\left(\lambda,\mu-\frac{1}{\sqrt{2}}\right)\times\psi_e\left(\lambda+\frac{1}{\sqrt{2}},\mu\right)\psi_e\left(\lambda,\mu+\frac{1}{\sqrt{2}}\right). \tag{55}$$

According to the general procedure presented in Sec. III C 2 based on Clebsch potentials, the appropriate initial data for the ARGLE method when $n_d=[\Gamma/(4\pi\alpha)]=4$ [see Eq. (49)] is given by

$$\psi(x,y)=\psi_4[\lambda(x,y),\mu(x,y)], \tag{56}$$

where λ and μ are defined in (53). For the two-dimensional test flow (52), the circulation around the box $[0,\pi]\times[0,\pi]$ is given by

$$\Gamma=\int_0^\pi\int_0^\pi dS\boldsymbol{\nabla}\times\mathbf{u}^{\mathrm{adv}}=4\int_0^\pi dx\ \sin(x)=8. \tag{57}$$

Thus the ratio of the total circulation to the elementary defect's circulation is $\gamma_d=8/4\pi\alpha=2/\pi\alpha$ with $\alpha=c\xi/\sqrt{2}$ [see

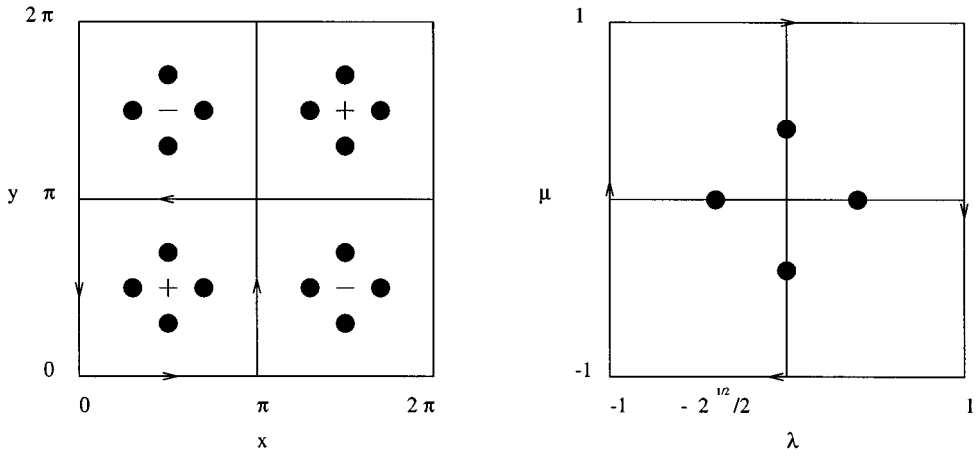

FIG. 3. Illustration of the mapping (53) between the physical and the (λ,μ) plane for the two-dimensional test flow (52). The dots represent the zeroes of (55) in the (λ,μ) plane and the corresponding vortices in physical space.

Eq. (22)]. As we want to consider only multiples of four defects, the final expression for the initial data for ARGLE reads

$$\psi(x,y)=\psi_4[\lambda(x,y),\mu(x,y)]^{[\gamma_d/4]}. \tag{58}$$

The function ψ corresponds to four multiple zeroes. The dynamics of a multiple zero under RGLE was studied in Ref. 7, which showed that a multiple zero of order n spontaneously splits into n simple zeroes of order 1. The same behavior is obtained under ARGLE dynamics (see Fig. 4).

2. Numerical results for energy spectra and spatial distribution of vortices: Minimization procedure

All of our numerical results are obtained using pseudospectral codes. The details of spectral representations and time-stepping schemes are explained in Appendix 1 and 2. In this section, the periodic box is $[0,2\pi]\times[0,2\pi]$.

Figure 4 shows the ARGLE converged field obtained with coherence length $\xi=0.1/(8\sqrt{2})$, sound velocity $c=2$, and resolution $N=512$, corresponding to $n_d=48$ and the initial data solution $\psi=\psi_4^{12}$. Each of the four, order-12, defects inside the box $[0,\pi]\times[0,\pi]$ has unfolded into 12 elementary vortices that have subsequently spread into the pattern shown in Fig. 4.

The corresponding ARGLE converged energy spectra are displayed in Fig. 5. It can be seen by inspection of Fig. 5(a) that, for wave numbers $k\geqslant 20$, the compressible kinetic energy is below the other energy spectra (except for a small region near the spectral cutoff $k_{\max}=N/2$). In the same wave number range, the energy spectra of incompressible kinetic energy $E^i_{\rm kin}$, quantum energy E_q, and internal energy $E_{\rm int}$ show the same overall features as the spectra of an isolated vortex computed in Sec. III B 2.

Figure 5(b) shows that the high wave number region of the incompressible momentum spectrum is well represented by the sum of 192 vortex spectra computed in Sec. III B 2. In contrast, for small wave numbers, the spectrum corresponding to the ARGLE converged system of vortices cannot be represented as a sum of independent vortex spectra. The separation between these two behaviors stems from the smallest distance between vortices. This distance can be estimated by counting on Fig. 6 16 vortices on the line $x=\pi/2$ which corresponds to a separation wavenumber $k_{\rm bump}\sim 16$.

The overall behavior of the ARGLE converged spectra displayed in Fig. 5 can be understood by analogy with the reproduction of a gray-scale picture, with ink dots (as done classically for engravings), the spatial density of the dots being taken to be proportional to the gray tone. The small wave number spectrum of the reproduction will be that of the original picture, while the large wave number spectrum will be that of the individual dots. Thus, the incompressible kinetic energy displayed in Fig. 5 contains two parts separated by $k_{\rm bump}$: the small k part is associated with the global motion corresponding to $\mathbf{u}^{\rm adv}$ and the high k part is associated with the individual vortices. The kinetic energy spectrum associated with $\mathbf{u}^{\rm adv}$ has the value 0.25 in the wave number shell corresponding to $k=1$ (see Appendix 3 for the definition of the wave number shells). The main contribution to the incompressible kinetic energy of the system of vortices is coming from the wave numbers $k\leqslant k_{\rm bump}$ and is found to have a value 0.251 511 close to the value 0.25 corresponding to $\mathbf{u}^{\rm adv}$. In this way, the ARGLE converged system of vortices mimics the imposed advective field $\mathbf{u}^{\rm adv}$ given by (52).

3. Numerical results for energy spectra and spatial distribution of vortices: Vorticity dynamics

Starting from the ARGLE converged system of vortices, the time evolution under NLSE dynamics (4) of the different components of the total energy is displayed in Fig. 7. The total energy is conserved throughout the run, with a relative maximum error at the end of the run of less than 0.2%. It can be also seen that the compressible kinetic and quantum energies remain small throughout the run, compared with the incompressible kinetic energy. The principal effect is a small oscillatory exchange between incompressible kinetic energy and internal energy. The angular velocity at the center $x=y=\pi/2$ of a vortex system is given by

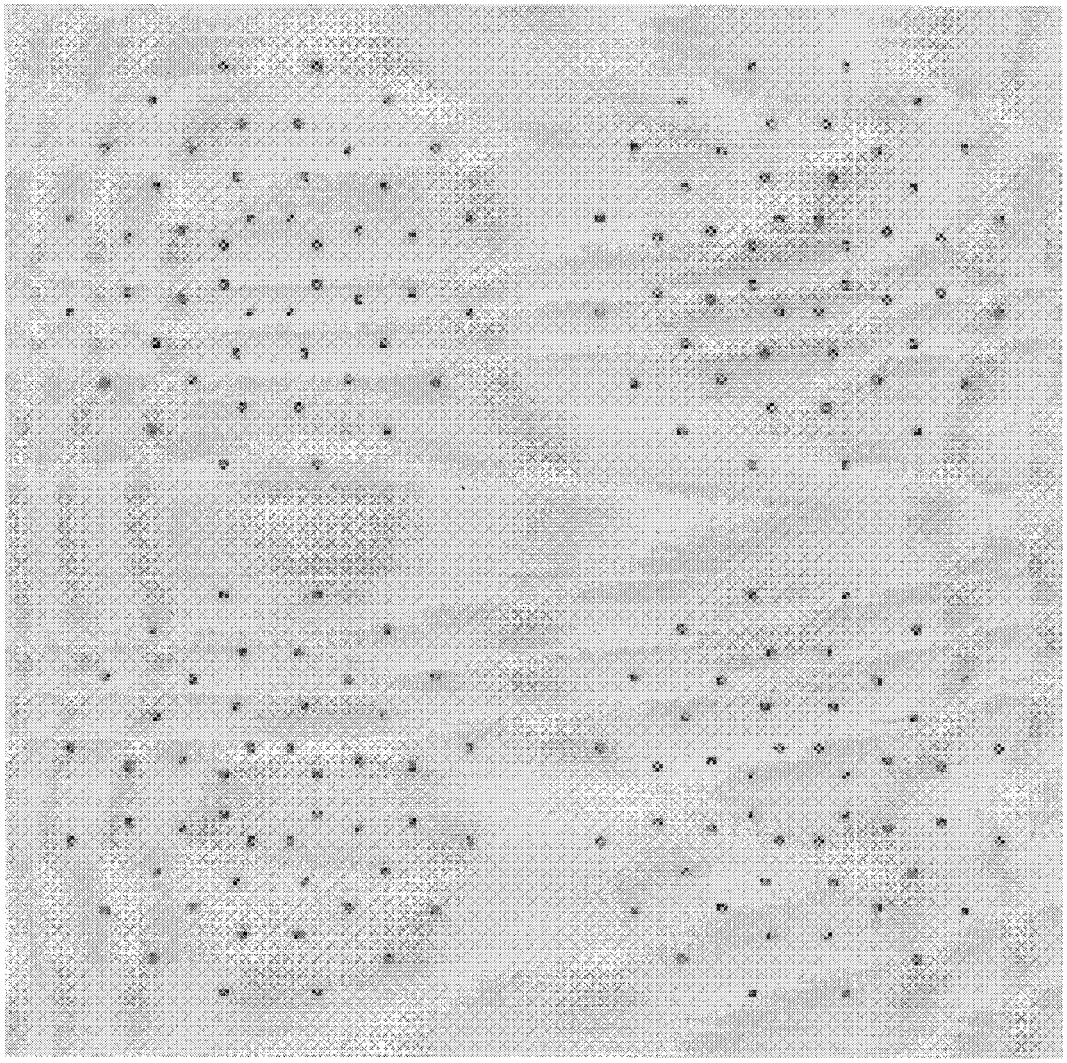

FIG. 4. A grey-scale plot of the initial condition density (ρ) for the two-dimensional test flow [Eq. (52)] with coherence length $\xi=0.1/(8\sqrt{2})$, sound velocity $c=2$, and resolution $N=512$. Each quarter of the periodicity box, mirror image of its neighbors, contains 48 point vortices rotating in the same direction.

$$\frac{1}{2}|\nabla\times\mathbf{u}^{\mathrm{adv}}|=1$$

in nondimensional units, which is of the same order of magnitude as the oscillation period. Although small compared to the incompressible kinetic energy, the compressible kinetic energy grows from 0.06% of the total energy to 2.17% at the end of the run. Thus a very small amount of acoustic emission has taken place.

The corresponding evolution in physical space is a differential rotation of each of the four vortex systems (with the sign of rotation shown on Fig. 3). The state at time $t=15$ is displayed in Fig. 6 which shows that the number of vortices remain constant. The energy spectra at time $t=15$ are displayed in Fig. 8. One of the main differences when compared to the spectra at time $t=0$ (see Fig. 5) is the growth of the compressible kinetic energy associated with the small amount of acoustic emission. The incompressible kinetic energy in the interval $1\leqslant k\leqslant k_{\mathrm{bump}}$, which corresponds to the large scales, decreases steeply. Indeed, a fit with a power law ($E^i_{\mathrm{kin}}=Ak^{-n}$) gives an exponent $n\sim 4.6$.

Finally, to close this section, we introduce and validate the procedures that will be used in the Sec. IV to measure the total length of vortices in the three-dimensional flow. For the simple two-dimensional test flow (52), these procedures consist merely of counting the total number of vortices, a constant throughout the run. We have used two different procedures:

(a) A fit of the incompressible momentum density spectrum J^i at high wave numbers (in the range $30\leqslant k\leqslant 170$) with the corresponding spectrum $J_{\mathrm{vort}}(k)$ of an individual vortex computed in Sec. III B 2 [see Fig. 1(b)]. The ratio of the integrals of the two spectra in the fitting range defines the number of vortices:

$$n_d=\frac{\Sigma_{k=30}^{170}J^i(k)}{\int_{30}^{170}J_{\mathrm{vort}}(k)dk}. \tag{59}$$

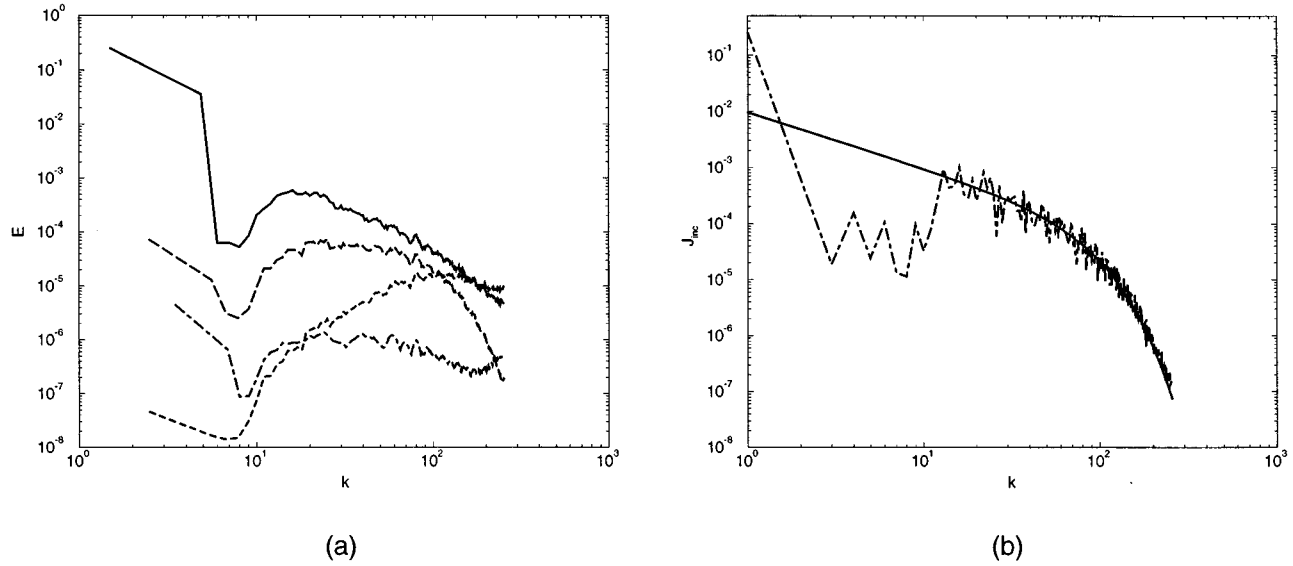

FIG. 5. Energy and incompressible momentum density spectra at time $t=0$ (same conditions as Fig. 4). (a) Incompressible kinetic energy $E^i_{\rm kin}$ (solid), compressible kinetic energy $E^c_{\rm kin}$ (dot-dashed), quantum energy E_q (dashed), and internal energy $E_{\rm int}$ (long–dashed). (b) Incompressible momentum density spectrum $J^i=(\rho\mathbf{v})_{\rm inc}$ (dot-dashed). Solid line is the momentum density spectrum of a single vortex [see Fig. 1(b)] multiplied by 192. Note that for wave numbers greater than $k_{\rm bump}\sim 16$ the two curves coincide.

We have checked that (data not shown) the value and the evolution of n_d do not change when the lowest value of the fit interval is varied, provided that it is of the order of (or larger than) $2k_{\rm bump}$.

(b) The ratio of the ''enstrophies'' which gives

$$n_d=\frac{\Sigma_{k=0}^{N/2}k^2J^i(k)}{\int_0^\infty k^2J_{\rm vort}(k)dk}. \tag{60}$$

The results of the two procedures are shown in Fig. 9 where it can be seen that, at large time, the fitting procedure (59) is somewhat more precise. As we will be comparing the results of the NLSE runs to the TG viscous incompressible ones, we will call in the remainder of the article the quantity $\Sigma_{k=0}^{N/2}k^2J^i(k)$ enstrophy.

The main result of this section is the global validation of our preparation and data analysis procedures. The vortex system has been shown to reproduce the Eulerian dynamics corresponding to a differential rotation with constant angular frequency. The amount of acoustic emission was found to be small and our vortex counting procedure was validated.

IV. NUMERICAL EVIDENCE FOR KOLMOGOROV TURBULENCE

The flow studied in this section — namely the Taylor–Green vortex defined below — is a reference flow in the numerical study of turbulence in the Navier–Stokes equations.[28]

A Clebsch representation of the Taylor–Green flow is given. This representation is used to generate a vortex-line array, whose ARGLE-converged nonlinear wave field obeys all the TG symmetries, and is well resolved numerically, including an exponential spectral falloff at high wave numbers.

This vortex-line array is used as an initial condition for NLSE simulations computed with a specialized pseudospectral code, making use of the TG symmetries to speed up the computations and optimize the memory size, which is described in Appendix 1.

We then compare the three-dimensional NLSE vortex dynamics, to previously published high-resolution simulations of the TG flow.[19–21] Evidence for Kolmogorov turbulence in NLSE is discussed.

A. Definition of the Taylor–Green flow and the associated vortex array

The TG flow is defined by the following advective velocity;

$$\begin{aligned} u_x^{\rm adv}(x,y,z)&=\ \sin(x)\cos(y)\cos(z),\\ u_y^{\rm adv}(x,y,z)&=-\cos(x)\sin(y)\cos(z),\\ u_z^{\rm adv}(x,y,z)&=0. \end{aligned} \tag{61}$$

Note that the solution of the incompressible Euler equation with initial data (61) has a vertical velocity component $u_z(x,y,z)\neq 0$ for $t\neq 0$. The flow that develops from (61) is thus a truly tridimensional flow. The TG flow was first introduced in Ref. 18 to study vortex stretching.

The Clebsch potentials

$$\begin{aligned} \lambda(x,y,z)&=\ \cos(x)\sqrt{2\,|\cos(z)|},\\ \mu(x,y,z)&=\ \cos(y)\sqrt{2\,|\cos(z)|}\ \mathrm{sgn}[\cos(z)], \end{aligned} \tag{62}$$

(where sgn gives the sign of its argument) correspond to the flow (61) in the sense that $\nabla\times\mathbf{u}^{\rm adv}=\nabla\lambda\times\nabla\mu$.

The mapping between physical space (x,y,z) and the (λ,μ) plane is displayed in Fig. 10. Only 1/8 of the total

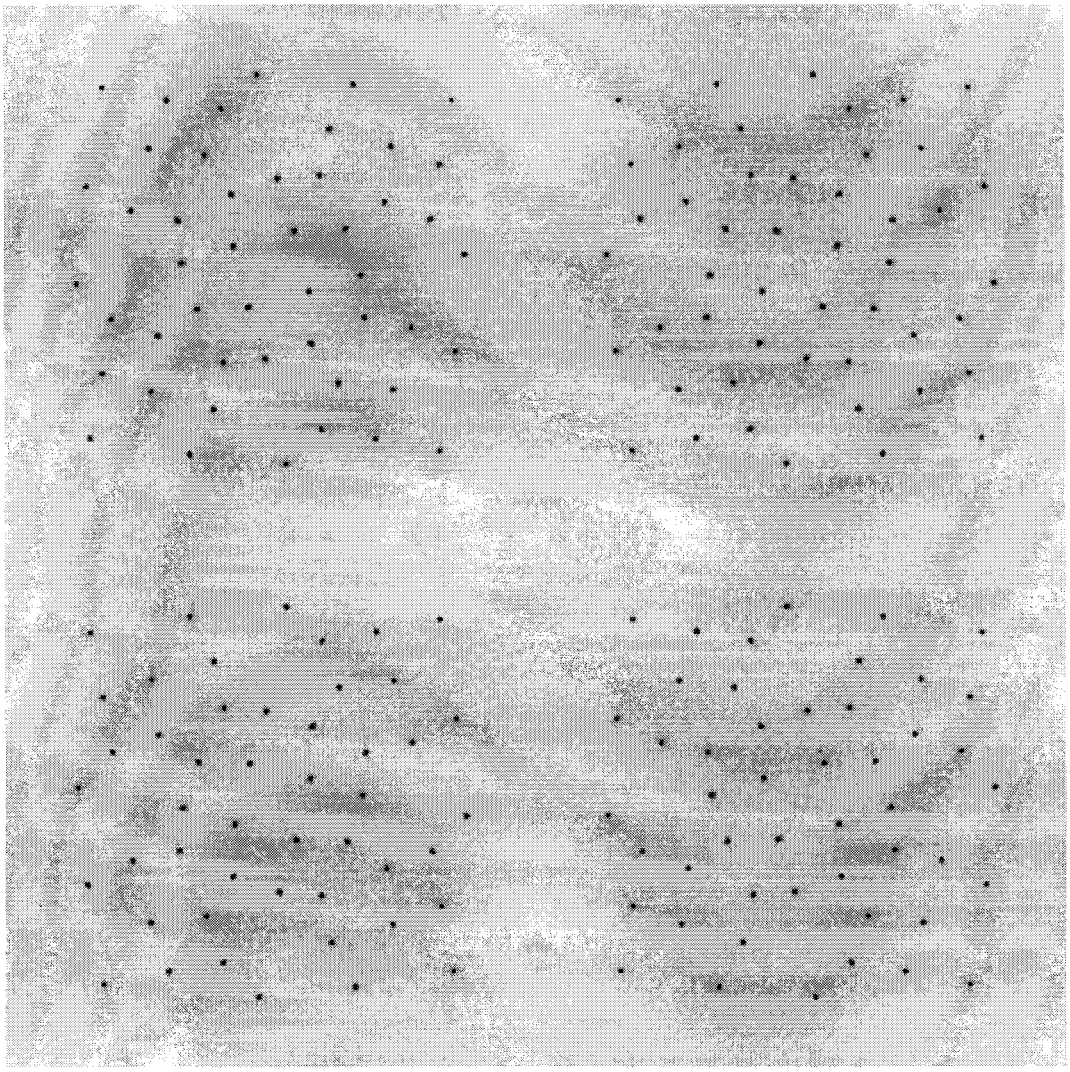

FIG. 6. Same as Fig. 4 but at time $t=15$. The number of vortices has remained constant.

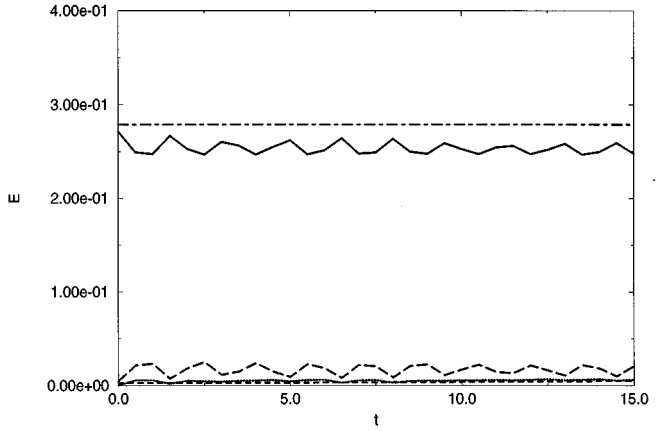

FIG. 7. Time evolution of total energy E_{tot} (dot-dashed), incompressible kinetic energy E^{i}_{kin} (solid line), compressible kinetic energy E^{c}_{kin} (dotted), quantum energy E_q (dashed), and internal energy E_{int} (long–dashed). Note the small oscillatory exchange between incompressible kinetic energy and internal energy while other energies remain negligible.

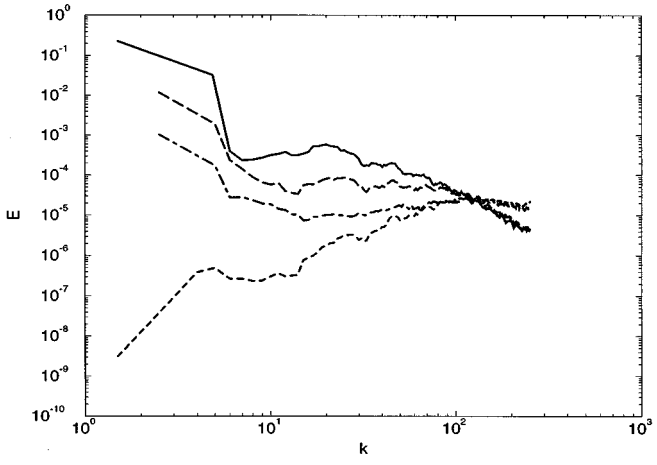

FIG. 8. Same as Fig. 5 (a) but at time $t=15$.

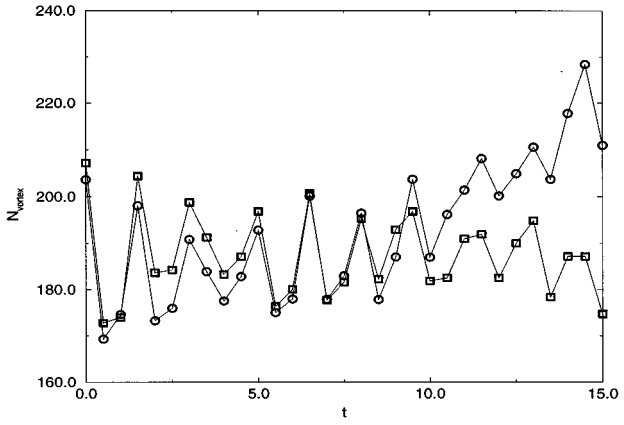

FIG. 9. Time evolution of the number of point vortices in the two-dimensional test flow (52) determined by two different procedures. (a) A fit of the incompressible momentum density spectrum (squares). The fit is performed for $30 \leqslant k \leqslant 170$, see Fig. 5(b). (b) The ratio of the total ''enstrophy'' and the enstrophy due to a single point vortex (circles). The fitting procedure (a) yields the original number of vortices (192) with an error of about 5%.

periodicity box $[0,2\pi]\times[0,2\pi]\times[0,2\pi]$ is shown on the left side of this figure. The rest of the field can be obtained by reflection in the boundaries of the picture. The extended vortex lines are thus closed vortex rings. The zeroes in the (λ,μ) plane are defined in the same way as in the two-dimensional test case [see Eqs. (54) and (55) and Fig. 3]. The appropriate initial data for the ARGLE method presented in Sec. III C 2 with $n_d=[\Gamma/(4\pi\alpha)]=4$ [see Eq. (49)] is given by

$$\psi(x,y,z)=\psi_4[\lambda(x,y,z),\mu(x,y,z)], \tag{63}$$

where λ and μ are defined in (62) and ψ_4 is the function defined in Eq. (55). For the TG flow (61), the circulation around the box $[0,\pi]\times[0,\pi]$ on the $z=0$ plane (see circuit $\mathscr{C}$ in Fig. 10) is given by

$$\Gamma=\int_0^\pi\int_0^\pi dS\,\boldsymbol{\nabla}\times\mathbf{u}^{\mathrm{adv}}=4\int_0^\pi dx\,\sin(x)=8. \tag{64}$$

Thus the ratio of the total circulation to the elementary defect's circulation is $\gamma_d=8/4\pi\alpha=2/\pi\alpha$ with $\alpha=c\xi/\sqrt{2}$ [see Eq. (21)]. The final expression for the initial data for ARGLE reads

$$\psi(x,y,z)=\psi_4[\lambda(x,y,z),\mu(x,y,z)]^{[\gamma_d/4]}. \tag{65}$$

Thus each line in Fig. 10 corresponds to a multiple zero line which, under ARGLE dynamics, will spontaneously split into $[1/2\pi\alpha]$ single zero lines (see Fig. 11).

These formulas, when restricted to $z=0$, are equivalent to the formulas (54), (55), (58) of the two-dimensional case. The presence of the $\sqrt{|\cos(z)|}$ factor in (62) is responsible for the curvature of the vortex lines seen in Fig. 10. It is shown in Appendix 1 that (65) is fully compatible with the symmetries of the TG flow.

B. Numerical results for the minimization procedure

Figure 11 shows a three-dimensional visualization of the ARGLE converged field obtained with coherence length $\xi=0.1/(8\sqrt{2})$, sound velocity $c=2$, and resolution $N=512$, corresponding to $n_d=48$ and the initial data solution $\psi=\psi_4^{12}$. The eight, order-12, lines (see Fig. 10) have unfolded and converged into the vortex array displayed in Fig. 11.

The corresponding ARGLE-converged energy spectra are shown in Fig. 12(a). They are remarkably similar to the spectra corresponding to the two-dimensional test flow (see Fig. 5). Figure 12(b) shows the incompressible momentum density spectrum $J^i(k)$. The high k part of this spectrum shows a conspicuous exponential decrease typical of a smooth well-resolved field. This proves that the ARGLE dynamics has rubbed out the lack of analyticity of the Clebsch initial data (62).

The radius of curvature of the vortex lines in Fig. 11 is large compared to their radius. Thus these three-dimensional lines can be considered as straight, and then compared to a collection of two-dimensional axisymmetric vortices inside the periodicity box $[0,2\pi]\times[0,2\pi]\times[0,2\pi]$. Indeed, for large wave numbers, the incompressible momentum density

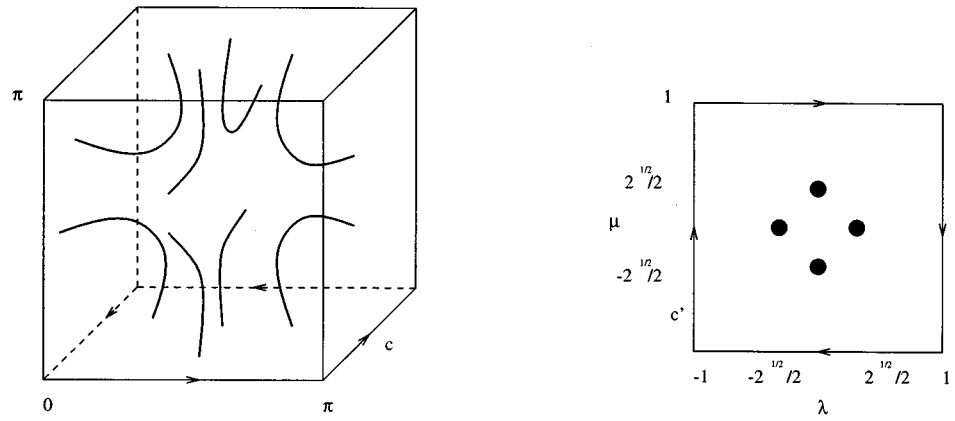

FIG. 10. Illustration of the mapping (62) between physical space and (λ,μ) plane for the Taylor–Green flow (61). The dots represent the zeros in the (λ,μ) plane corresponding to vortex lines in physical space. Note that only 1/8 of the total periodicity box $[0,2\pi]\times[0,2\pi]\times[0,2\pi]$ is shown on the left. The rest of the field can be obtained by mirror reflection in the boundaries of the picture. The vortex lines are thus closed rings.

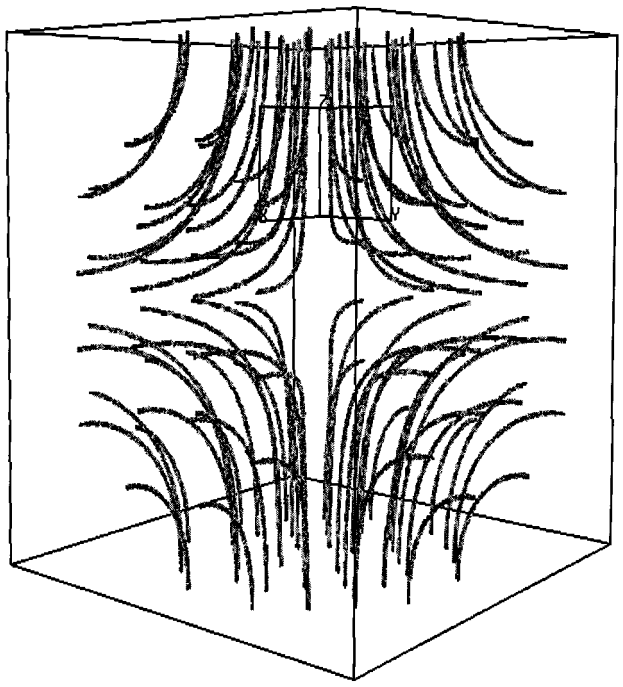

FIG. 11. Three-dimensional visualization of the vector field $\nabla\times(\rho\mathbf{v})$ of the initial data for the Taylor–Green flow with coherence length $\xi=0.1/(8\sqrt{2})$, sound velocity $c=2$, and $N=512$ in the impermeable box $[0,\pi]\times[0,\pi]\times[0,\pi]$. Direction of vector field at each point is indicated by orientation of small rods.

spectrum $J^i(k)$ of Fig. 12(b) is well represented by multiplying the spectrum $J_{\rm vort}(k)$ of a single two-dimensional point vortex by a factor,

$$\frac{l}{2\pi}=\frac{\Sigma_{k=30}^{170}J^i(k)}{\int_{30}^{170}J_{\rm vort}(k)\ dk}. \tag{66}$$

This constant of proportionality is related to the length l of the three-dimensional vortex lines and to the length 2π of a single two-dimensional point vortex seen in the three-dimensional periodicity box of side 2π. This factor (66) is then equal to the total number of three-dimensional vortex lines [just as it is equal to the total number of point vortices in the two-dimensional test flow, see (59) and the comment below]. This fitting procedure allows us to determine the total length of vortex lines l.

We have performed a series of ARGLE runs corresponding to various resolutions, and parameters are summarized in Table I. Here and in the remainder of the article, the velocity of sound is set to $c=2$ unless otherwise specified.

Table I shows that, as ξ decreases (which requires an increase in resolution), the incompressible kinetic energy converges towards the value 0.125 associated with the TG vortex (61). The other energies decrease as the resolution increases.

On the other hand, the total vortex length l and the total enstrophy increase. These two quantities are related [see (60)]. The length l can also be defined (although in a somewhat less precise way, see Fig. 9) as the ratio of the enstrophies:

$$\frac{l}{2\pi}=\frac{\Sigma_{k=0}^{N/2}k^2J^i(k)}{\int_0^{\infty}k^2J_{\rm vort}(k)\ dk}. \tag{67}$$

The main conclusion that can be drawn from inspection of Table I is that our initial data preparation method described in Sec. III C constructs vortical flows whose incompressible kinetic energy converges towards the nominal TG value 0.125 as ξ decreases, while the other components of the energy tend to zero. In contrast, in this limit, the total enstrophy

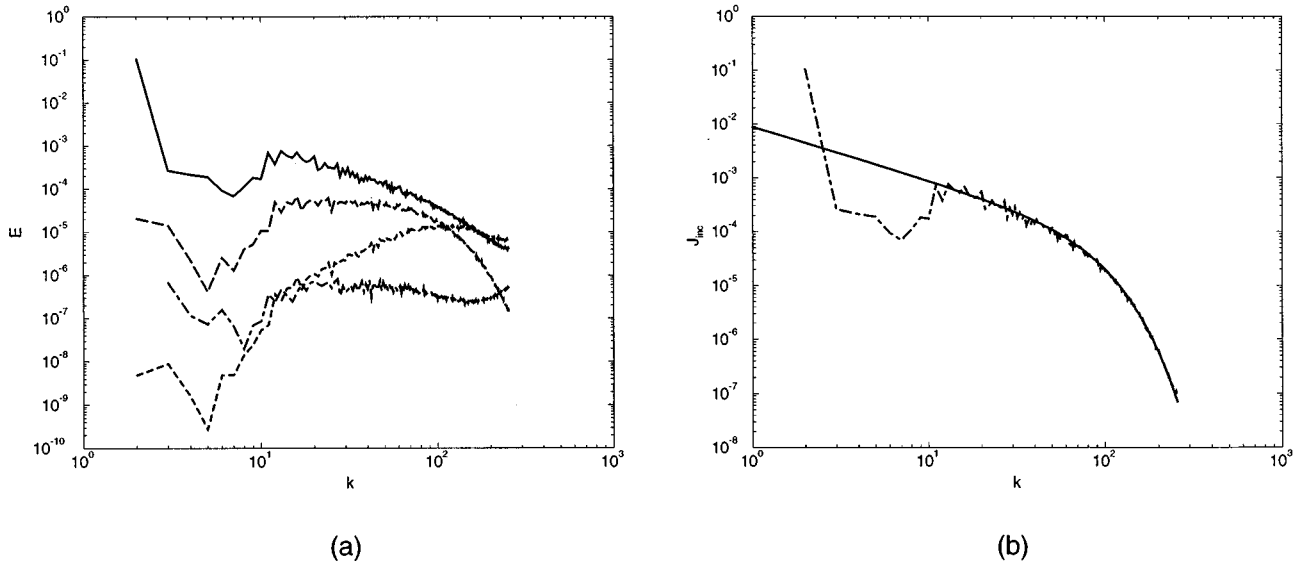

FIG. 12. Energy and incompressible momentum density spectra at time $t=0$ (same conditions as Fig. 11). (a) Incompressible kinetic energy $E^i_{\rm kin}$ (solid), compressible kinetic energy $E^c_{\rm kin}$ (dot-dashed), quantum energy E_q (dashed), and internal energy $E_{\rm int}$ (long–dashed). (b) Incompressible momentum density spectrum. Solid line is the momentum density spectrum of a single two-dimensional point vortex [Fig.1(b) multiplied by a factor $l/(2\pi)$] determined by a fit at high k. This fitting procedure leads to the total vortex length in the periodicity box [see text, Eq. (59)].

TABLE I. Characteristics of the ARGLE runs that will be used as initial data for the NLSE dynamics. The values of the energies, enstrophy, and vortex length are indicated at the final time $t=T_{\mathrm{ARGLE}}$.

Run	a	b	c	d
Resolution	128	256	400	512
ξ	$0.1/(2\sqrt{2})$	$0.1/(4\sqrt{2})$	$0.1/(6.25\sqrt{2})$	$0.1/(8\sqrt{2})$
T_{ARGLE}	60	60	15	60
dt_{ARGLE}	0.025	0.0125	0.008	0.006 25
E^i_{kin}	0.129 022	0.129 603	0.126 182	0.124 262
E^c_{kin}	0.000 488	0.000 26	0.000 358	0.000 129
E_q	0.007 925	0.004 598	0.003 173	0.002 382
E_{int}	0.013 004	0.007 772	0.005 444	0.004 099
Enstrophy	6.357 064	14.544 741	24.084 934	30.105 943
$l/2\pi$	36.584 050	83.703 032	138.605 561	177.864

$\Sigma_{k=0}^{N/2} k^2 J^i(k)$ increases with the total length of vortices. The large value of l in run d is related to the large number of lines present in Fig. 11.

The increase of the total vortex length l with the resolution can be estimated by the following argument. In order to maintain accuracy, when ξ is decreased, N is increased as $(N/2\pi)\sim 0.72\times\xi^{-1}$. Using (22), we obtain $\alpha\sim(c/\sqrt{2})\times(2\pi/N)\times 0.72$. Note that $l/2\pi$ defined in (66) is the number of defect lines crossing the $z=0$ plane inside the $[0,2\pi]\times[0,2\pi]$ (x,y) box. This number is four times the number of defects inside the $[0,\pi]\times[0,\pi]$ box, given by $8/4\pi\alpha$ [see (64) and (65)]. Thus the total vortex length increases with the resolution as

$$\frac{l}{2\pi}\sim\frac{32N}{(2\pi)^2\sqrt{2}c\times 0.72}. \tag{68}$$

In order to check that the runs of Table I are adequately resolved, we have compared the results of several ARGLE runs with different resolutions but the same values of c and ξ. Table II shows that the $N=128$ run corresponding to a value of $\xi/\Delta x=0.72$ (where $\Delta x=2\pi/N$ denotes the mesh size), is well converged. It is this value of $\xi/\Delta x$ that has been used in all the other runs presented in this paper. That this resolution is adequate is confirmed by inspection of the spectrum of Fig. 12(b) showing an exponential tail for most of the large-k regime.

TABLE II. Characteristics of the ARGLE runs used to check resolution.

Run	j	a'	k
Resolution	64	128	256
ξ	$0.1/(2\sqrt{2})$	$0.1/(2\sqrt{2})$	$0.1/(2\sqrt{2})$
T_{ARGLE}	30	30	30
dt_{ARGLE}	0.05	0.025	0.0125
E^i_{kin}	0.128 984	0.129 041	0.129 570
E^c_{kin}	0.011 971	0.000 488	0.000 272
E_q	0.087 639	0.007 926	0.007 804
E_{int}	0.401 425	0.013 005	0.013 028
Enstrophy	9.749 363	6.357 759	6.356 975
$l/2\pi$	56.106 275	36.588 050	36.583 538

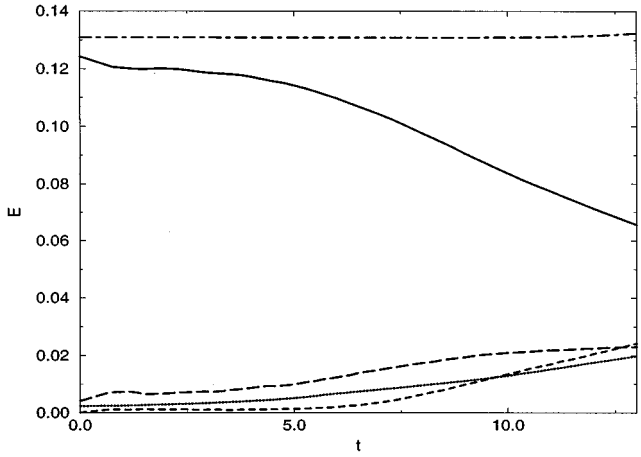

FIG. 13. Time evolution of total energy E_{tot} (dot-dashed), incompressible kinetic energy E^i_{kin} (solid), compressible kinetic energy E^c_{kin} (dotted), quantum energy E_q (dashed), and internal energy E_{int} (long–dashed) for run d. Note the transfer of energy from the incompressible part to the other contributions.

C. Numerical results for the vorticity dynamics

Perhaps the most striking result of the three-dimensional vortex dynamics is that NLSE dynamics manages to transfer a sizeable amount of the flow's incompressible kinetic energy into other energy components. This behavior is displayed in Fig. 13 which shows the time evolution of the different components of the total energy for run *d*. In sharp contrast with the two-dimensional vortical flow evolution shown in Fig. 6, an irreversible transfer of incompressible kinetic energy into compressible kinetic, quantum, and internal energies is manifest in Fig. 13.

One of the main quantitative results of this article is the excellent agreement of the incompressible kinetic energy dissipation rate shown on Fig. 14(b) with the corresponding data in the incompressible viscous TG flow [Ref. 19, Fig. 7, Ref. 21, Fig. 1(b), and Ref. 28, Fig. 5.12]. Both the time for maximum energy dissipation $t_{\mathrm{max}}\sim 5$–10 and the value of the dissipation rate at that time $\epsilon(t_{\mathrm{max}})\sim 10^{-2}$ are in quantitative agreement.

In the limit of decreasing ξ, the coordinates $(t_{\mathrm{max}},\epsilon(t_{\mathrm{max}}))$ of the maximum energy dissipation show a weak dependence on ξ. This is remarkably similar to the weak dependence of the corresponding viscous quantity in the limit of viscosity ν going to zero. In the viscous case, the weak dependence in ν of $\epsilon(t_{\mathrm{max}})$ is considered a hallmark of numerical evidence for a Kolmogorov regime in decaying turbulence.[28] By inspection of Fig. 14(b) for run *d*, $t_{\mathrm{max}}\sim 8$, while the first inflection point of $\epsilon(t)$ is in the range $4<t<5$ and corresponds on Fig. 14(a) to the beginning of an appreciable decrease of the incompressible kinetic energy. This change of behavior is probably linked to the vortex reconnections that begin at $t\sim 5$ (see following).

Another important quantity studied in viscous decaying turbulence is the scaling of the kinetic energy spectrum dur-

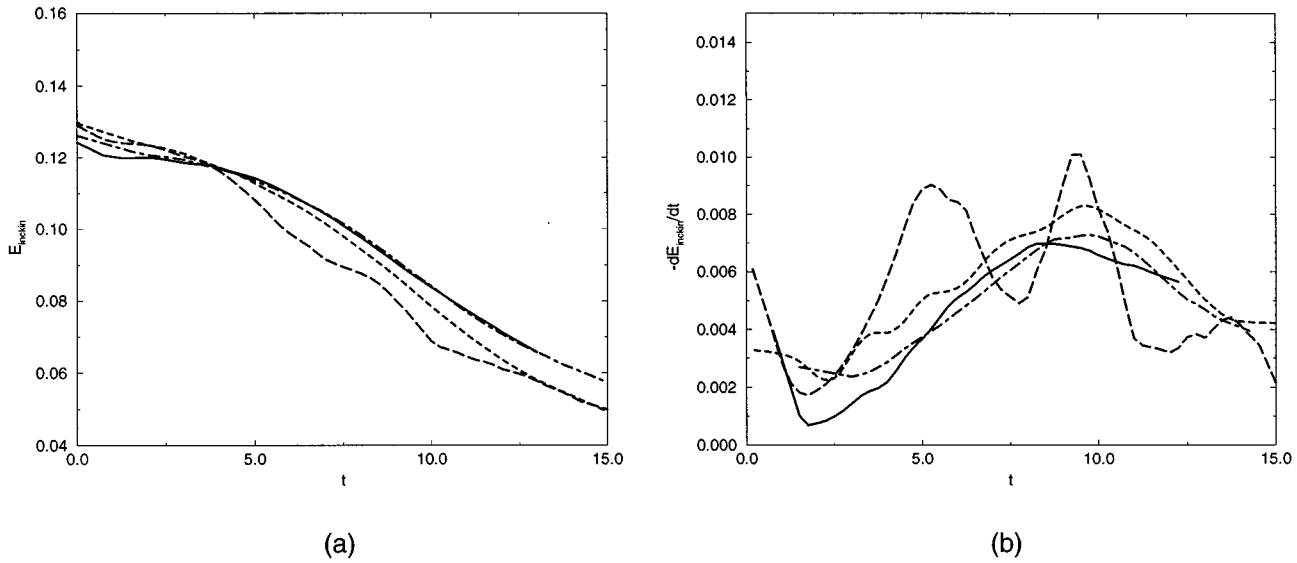

FIG. 14. Evolution of the total incompressible kinetic energy in the Taylor–Green flow: run a with $\xi=0.1/(2\sqrt{2})$ and $N=128$ (long–dashed), run b with $\xi=0.1/(4\sqrt{2})$ and $N=256$ (dashed), run c with $\xi=0.1/(6.25\sqrt{2})$ and $N=400$ (dot-dashed) and run d with $\xi=0.1/(8\sqrt{2})$ and $N=512$ (solid). Figure 14(a) shows $E^i_{\rm kin}$ and Fig. 14(b) the associated dissipation $-dE^i_{\rm kin}/dt$. Note that $E^i_{\rm kin}$ becomes independent of ξ as ξ decreases and that the time of maximum dissipation $t_{\rm max}$ is shifted from $t_{\rm max}\sim 6$ for run a to $t_{\rm max}\sim 10$ for other runs.

ing time evolution, particularly at the time of maximum energy dissipation where a $k^{-5/3}$ range can be observed (see Ref. 19, Fig. 16).

The time evolution of the energy spectra in the NLSE case are displayed in Fig. 15. One can observe a small k buildup of the incompressible kinetic energy spectra and a high k buildup of the compressible kinetic energy spectra. The overall effect of the energy transfers at large time (see Fig. 15) is that a part of the large-scale original incompressible kinetic energy has fed the other energy components at higher wave numbers. In the same way as explained in the two-dimensional case (see discussion in Sec. III D 2), the high k region, $k\geqslant k_{\rm bump}\sim 16$, of all the energy spectra (except the compressible kinetic energy spectrum) can be attributed to the contribution of the individual vortex lines. The small k region, $k\leqslant k_{\rm bump}\sim 16$, is associated with motion at scales larger than the vortex lines separation. The evolution in time of the exponent $n(t)$ of the spectral fit $E^i_{\rm kin}=A(t)k^{-n(t)}$ is displayed in Fig. 16(a) for different spectral fitting intervals. It can be seen on Fig. 16(a) that the spectral exponent is comparable with the Kolmogorov value $n=5/3$ for times close to $t_{\rm max}$. An example of a fit in this regime is given in Fig. 16(b). Note that a similar fit performed at the end of the NLSE run in the two-dimensional test flow gave a much steeper exponent of 4.6 (see Sec. III D 3). Although the fits were actually performed on very narrow wave number intervals, it is tempting to speculate on the scalings that would be observed with a larger value of $k_{\rm bump}$ than the one we can reach with our maximum resolution. First, let us remark that a fit done on an interval at the right of $k_{\rm bump}$ would yield $n\sim 1$, the correct value for an isolated vortex (see the discussion at the end of Sec. III B 2). This might explain the systematic lower value for the computed $n(t)$ when the fit range is increased up to $k_{\rm bump}\sim 16$. Second, it can be seen on Fig. 16 that this systematic deviation undergoes a sharp decrease after $t\sim 4$. This might be related to the onset of vortex reconnection (see following). We thus speculate that it is not unreasonable to expect to find Kolmogorov scaling within that range in an asymptotic regime where $k_{\rm bump}$ is much larger than the integral scale wave number.

A striking difference between the behavior of the three-dimensional NLSE dynamics spectra and the two-dimensional vortical flow spectra is the evolution of the total length of vortices in the three-dimensional flow. In contrast to the corresponding two-dimensional quantity, namely the number of point vortices defined through Eq. (59) or Eq. (60) that remain almost constant in time (see Fig. 9), the three-dimensional total length of vortices defined through Eq. (67) or Eq. (66) displays an increase in time by a factor 3 as shown in Fig. 17. This difference of behavior between the two- and the three-dimensional cases can be related to vortex stretching, classically present in the three-dimensional case and absent in the two-dimensional case.

The early time behavior of the vortex lines is shown in Figs. 18(a) and 18(b). It can be seen by inspection of these figures that the vortex lines have been distorted but no reconnection has yet taken place.

The standard classical argument concerning vortex stretching by a large scale incompressible flow can be extended to an assembly of parallel NLSE vortex lines. If a cylinder of base, s_1, and length, L_1, containing n vortex lines parallel to its generators, is stretched along the vortex lines by a large-scale incompressible flow into a cylinder of base, s_2, and length, L_2, volume conservation implies that $s_1L_1=s_2L_2$ with $s_2<s_1$ and $L_2>L_1$. Thus a large-scale stretching is trivially accompanied by an increase of total length of NLSE vortices. Note that this is a property of the *collection* of NLSE vortices: an individual vortex line, when stretched,

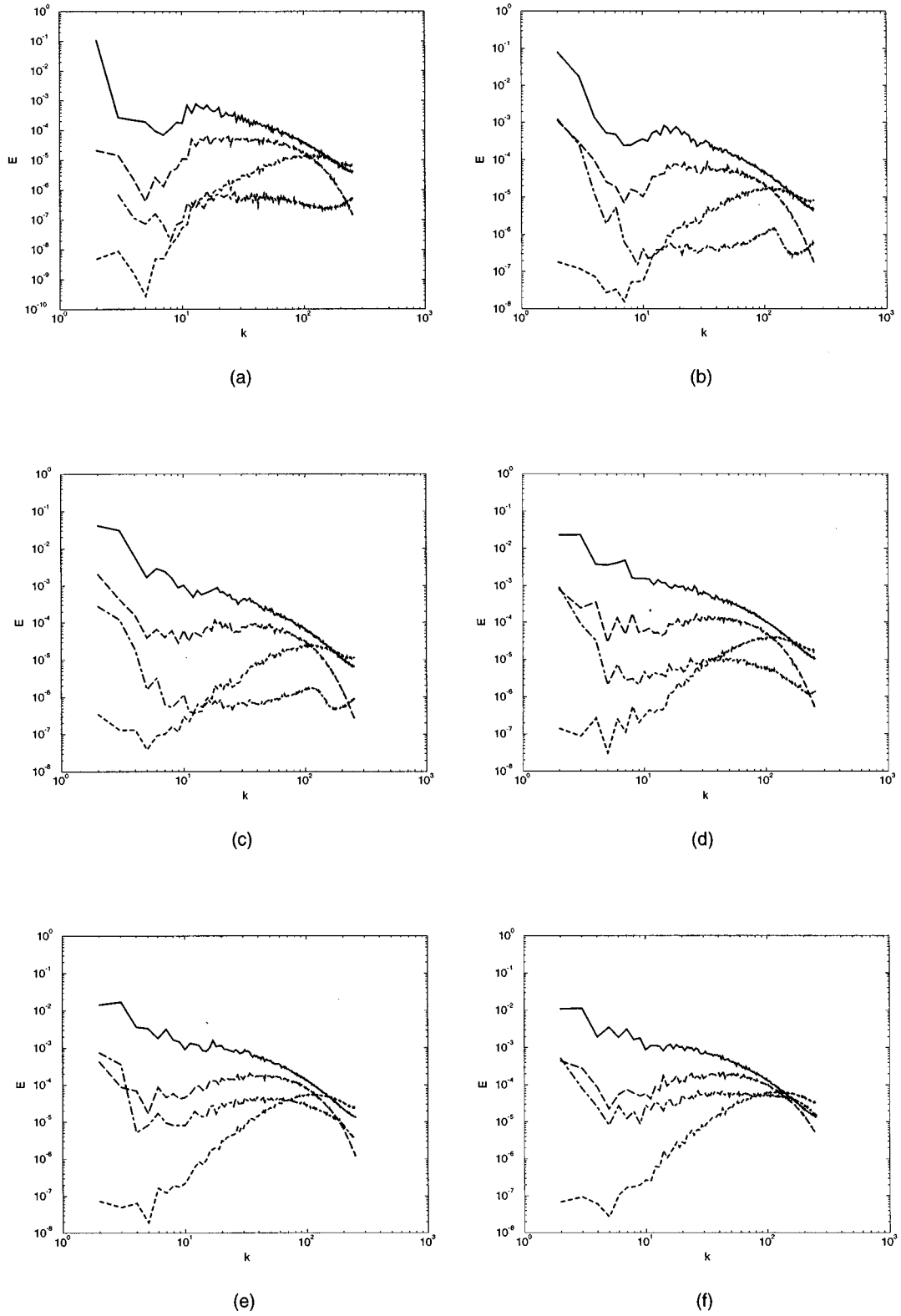

FIG. 15. Energy spectra for run d: incompressible kinetic energy $E^i_{\rm kin}$ (solid), compressible kinetic energy $E^c_{\rm kin}$ (dot-dashed), quantum energy E_q (dashed), and internal energy $E_{\rm int}$ (long–dashed). (a) $t=0$; (b) $t=2$; (c) $t=4$; (d) $t=6$; (e) $t=8$, and (f) $t=10$. Note the transfer of incompressible energy towards other energies and the buildup of the compressible kinetic energy spectrum at large k.

keeps its circulation $4\pi\alpha$ *and* its typical diameter ξ constant, whereas the diameter of the collection decreases and thus the vortex line density increases.

Consequently, the short time $(0\leqslant t\leqslant 4)$ increase of total vortex lines seen in Fig. 17 can be related to the vortex stretching classically present in the TG vortex. Indeed the global flow evolution seen in Figs. 18(a) and 18(b) is identical to the early time inviscid dynamics dominated by vortex

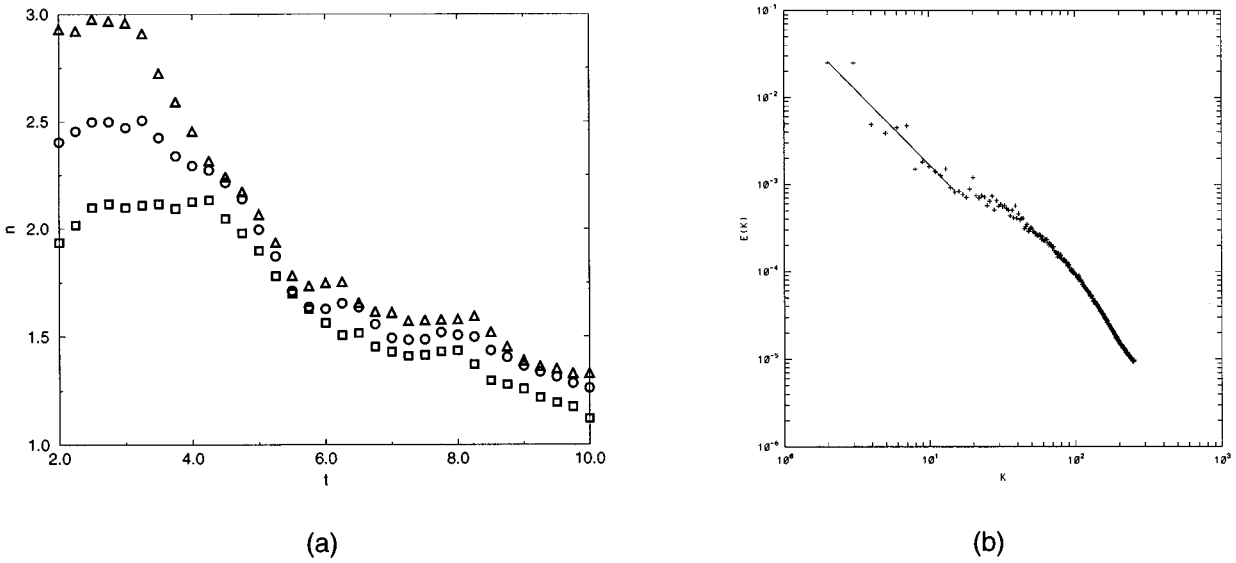

FIG. 16. Exponent $n(t)$ in the spectral fit $E^i_{\rm kin}(k)=A(t)k^{-\,n(t)}$ for run d. (a) Compares $n(t)$ computed from least-square fits over wave number intervals $2\leqslant k\leqslant 12$ (triangles), $2\leqslant k\leqslant 14$ (circles), and $2\leqslant k\leqslant 16$ (squares). (b) Solid line shows least-square fit over $2\leqslant k\leqslant 16$ at time $t=5.5$ [with $A(5.5)=0.08$ and $n(5.5)=1.70$].

stretching near the walls of the impermeable box which is described in Refs. 19 and 31. Such a similarity is not surprising since it can be demonstrated that isolated NLSE vortex lines follow Eulerian dynamics.[8] Thus the short time evolution of the NLSE flow mimics the continuous Eulerian flow in the same way that classical vortex line element methods are used to simulate Euler equations.[32,33]

However, this analogy cannot cope with vortex reconnection. Indeed it is well known that the main limitation of vortex line element methods is that the calculation must be stopped, after a finite time, when too much stretching takes place at some location.

Detailed visualizations of the NLSE results (data not shown) show that many reconnections take place throughout the flow after $t\sim 5$. The resulting rather intricate vortex line tangle is shown in Figs. 18(c), 18(d), 18(e), and 18(f). Note that, in the evolution of the viscous TG vortex,[19] there is also a qualitative (and a quantitative) change in vortex dynamics around $t\sim 5$.

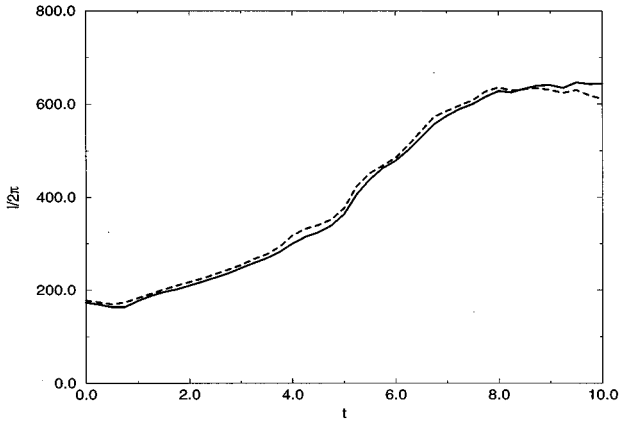

FIG. 17. Vortex filament length divided by 2π in run d. This length is determined by the two procedures illustrated in Fig. 9. Solid and dashed curves show results of procedure (a) (59) and procedure (b) (60), respectively. Because of vortex stretching, the total length has increased by a factor of 3, in contrast to the two-dimensional case.

Because of the high complexity of the vortex tangle for $t\geqslant 5$, it is convenient to define a space-averaged quantity, ω_f, which is the curl of the filtered momentum density, $(\rho v_j)_f$, defined as follows:

$$(\widehat{\rho v_j})_f(k) = \begin{cases} (\widehat{\rho v_j})_f(k) & \text{for } k_x\leqslant k_{\max},\ k_y\leqslant k_{\max},\ k_z\leqslant k_{\max} \\ & (\text{with } k_{\max}=16) \\ 0, & \text{otherwise.} \end{cases}$$

The isosurfaces of ω_f that are displayed in Fig. 19 can be directly compared to Fig. 16–19 of Ref. 19. Both the NLSE and the viscous figures show a similar evolution of the spatial localization of turbulent activity. At $t=5$, the activity is localized within vortices close to the midsection $z=\pi/2$ of the walls $(x=y=0,\pi)$ of the impermeable box $x=0,\pi$, $y=0,\pi$, $z=0,\pi$. In both cases, after a transient at $t\sim 6$, the turbulent activity spreads into a substantial fraction of the impermeable box. As discussed in detail in Ref. 19, it is known that viscous reconnection processes are of prime importance in understanding the complex later-time dynamics in the TG vortex.

The similarity of the energy transfer and spectral behavior between the NLSE and viscous TG vortices in the interval $5\leqslant t\leqslant 10$ (see Figs. 14 and 16 together with their corre-

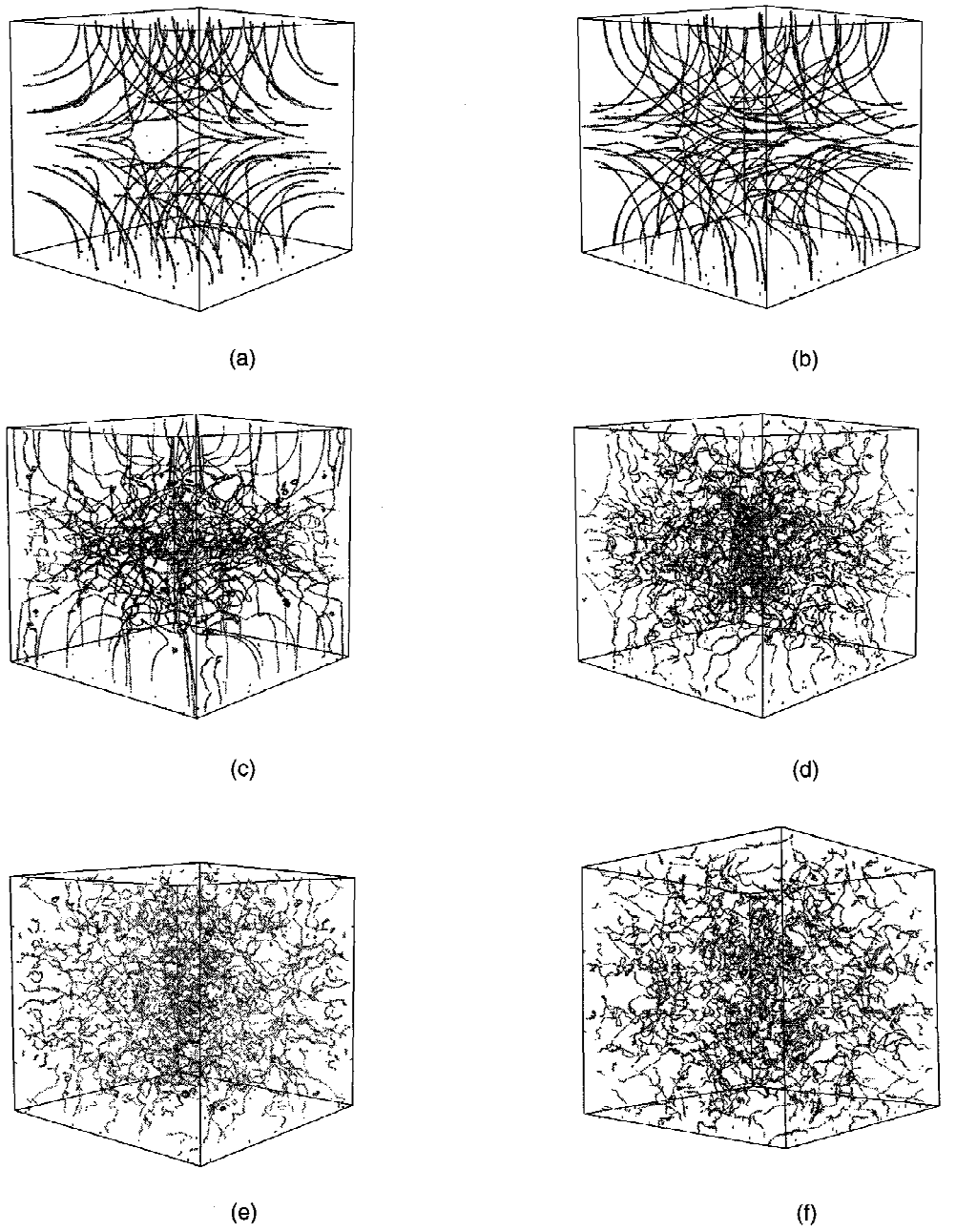

FIG. 18. Three-dimensional visualizations of $\nabla\times(\rho\mathbf{v})$ for the Taylor–Green flow at various times with coherence length $\xi=0.1/(8\sqrt{2})$ and $N=512$ in the impermeable box $[0,\pi]\times[0,\pi]\times[0,\pi]$: (a) $t=2$; (b) $t=4$; (c) $t=6$; (d) $t=8$; (e) $t=10$; and (f) $t=12$.

sponding Figs. 7 and 9 in Ref. 19) is thus quite remarkable. A possible tentative interpretation could be that, although vortex line reconnection is necessary to reach this late-time regime, the detailed physical reconnection mechanisms are largely irrelevant. This would explain the observed quantitative similarity of the overall depletion of incompressible kinetic energy, despite the obviously different viscous and dispersive reconnection processes.

D. Discussion

As seen in the previous section, the spectral behavior of NLSE can be compared to viscous turbulence only for $k \leqslant k_{\mathrm{bump}}$. It is thus of interest to estimate the scaling of k_{bump} in terms of the characteristic parameters of the large scale flow and of the fluid. It was noted, in Sec. III D 2, that $k_{\mathrm{bump}}\sim d_{\mathrm{bump}}^{-1}$, where d_{bump} is the average distance between neighbor vortices. The flow parameters are the characteristic integral scale l_0 (with corresponding wave number $k_0 \sim l_0^{-1}$) and the characteristic large-scale velocity u_0 which are, in the case of the TG flow, $l_0\sim 1$ and $u_0\sim 1$. The fluid characteristics are the sound velocity c and the coherence length ξ (with corresponding wave number $k_\xi\sim\xi^{-1}$). Using the expression (49) for the number of defects n_d and the relation $\Gamma\sim l_0 u_0$, one finds

$$n_d\sim\frac{l_0 u_0}{c\xi}. \tag{69}$$

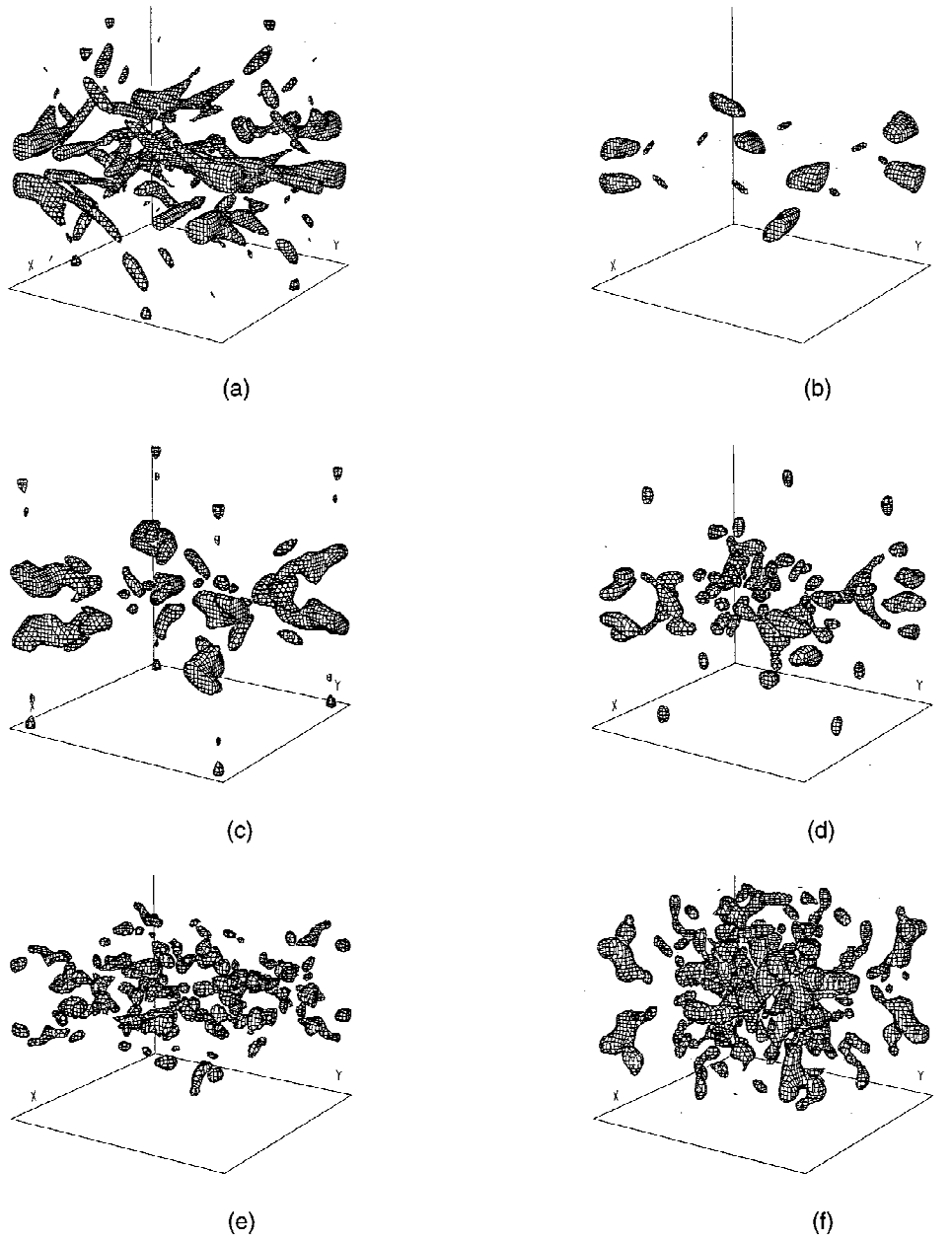

FIG. 19. Three-dimensional perspective plots of volumes in which $|\omega_f|^2 \geqslant 0.6\ |\omega_f|^2_{\max}$, where ω_f is the curl of the filtered momentum density $(\rho v_j)_f$ (see text). Parameters as in Fig. 18; (a) $t=4$, (b) $t=5$, (c) $t=6$, (d) $t=7$, (e) $t=8$, and (f) $t=9$.

Assuming that the vortices are uniformly spread over the large scale area l_0^2, one obtains

$$n_d \sim \frac{l_0^2}{d_{\text{bump}}^2}. \tag{70}$$

Equating these two evaluations of n_d yields the relation

$$d_{\text{bump}} \sim \sqrt{(c/u_0)\xi l_0}, \tag{71}$$

or, in terms of wave numbers and Mach number $M=u_0/c$,

$$k_{\text{bump}} \sim \sqrt{M k_0 k_\xi}. \tag{72}$$

At a given value of the Mach number and of the integral scale, Eq. (72) shows that the range over which NLSE behavior can be compared to viscous turbulence increases as $\sqrt{k_\xi}$. However, when running a numerical computation, one must fix k_0 to the smallest wave number and k_ξ to the largest. Thus, the range is in fact limited by $\sqrt{M k_0 k_\xi}$, and, in order to maximize it, M should as large as possible. However, M is bounded by the requirement that acoustic waves generated by compressibility do not dominate the dynamics.

1. Compressibility effects

All the vorticity dynamics results presented so far were performed with $c=2$ corresponding to a rms Mach number, $M_{\text{rms}} \equiv |\mathbf{u}^{\text{adv}}_{\text{rms}}|/c = 0.25$. It is known that, in compressible turbulence, the compressibility effects become noticeable for $M_{\text{rms}} \geqslant 0.3$.[34] In the present study, we have compared the NLSE results with the published incompressible viscous TG

results. An interesting project, that is left for further study, would be to compare the NLSE results, at a given rms Mach number, with the corresponding *compressible* viscous TG vortex. In order to ascertain compressibility effects in the NLSE simulations, we have performed several runs at $N=256$ and $\xi=0.1/(2\sqrt{2})$, with various values of $M_{\rm rms}$.

Table III shows the effect of variation of the rms Mach number on the ARGLE converged results. The principal effect of decreasing $M_{\rm rms}$ is to decrease the total vortex length l. The incompressible kinetic energy is almost constant while the compressible kinetic energy is negligible. The quantum and internal energies, although small, are seen to increase when $M_{\rm rms}$ goes to zero.

As it is very costly to decrease the $M_{\rm rms}$ while maintaining the number of vortices constant, we checked that compressibility effects would dominate for $M_{\rm rms}\geqslant 0.3$. The energy dissipations corresponding to Table III are displayed in Fig. 20. It can be seen on this figure that the maxima of dissipation corresponding to $M_{\rm rms}=0.5$ and $M_{\rm rms}=0.33$ occur at earlier times (respectively, 2 and 5) than those corresponding to $M_{\rm rms}=0.25$ and $M_{\rm rms}=0.125$ (respectively, 10 and 7). Thus, for $M_{\rm rms}\geqslant 0.25$, compressibility effects are seen to affect the early time dynamics. This is why the value of $M_{\rm rms}=0.25$ was used as a compromise in the high resolution computations of Sec. IV.

TABLE III. Characteristics of the ARGLE runs with $N=256$ and $\xi=0.1/(4\sqrt{2})$.

Run	*e*	*f*	*b*	*g*
c	1	1.5	2	4
$M_{\rm rms}$	0.5	0.33	0.25	0.125
$T_{\rm ARGLE}$	60	60	60	60
$dt_{\rm ARGLE}$	0.0125	0.0167	0.0125	0.0125
$E^i_{\rm kin}$	0.122 360	0.125 479	0.129 603	0.140 687
$E^c_{\rm kin}$	0.000 756	0.000 265	0.000 26	0.000 273
E_q	0.002 582	0.003 598	0.004 598	0.007 597
$E_{\rm int}$	0.004 560	0.006 008	0.007 772	0.013 079
Enstrophy	8.573 721	11.596 907	14.544 741	23.687 039
$l/2\pi$	197.362 453	118.646 476	83.703 032	34.078 932

2. Evidence for universality of reconnection processes

The number and complexity of the reconnection events leading from the simple ordered state displayed in Fig. 18(a) to the complex vortex tangle shown in Fig. 18(f) is so great that a detailed understanding of its formation seems impossible. We were led in the previous section to speculate that there should be a certain amount of universality between Navier–Stokes reconnection processes and NLSE reconnection processes. In this section, we test this hypothesis on a simpler flow where reconnection events are tractable.

It is well known, both experimentally[35] and numerically using the Navier–Stokes equations,[36] that the secondary instability of three-dimensional round jets leads to the formation of sidejets. The formation of the primary (Kelvin–Helmoltz) instability and the early onset of the secondary instability (when pairs of axially counter-rotating vortex filaments appear) can be explained by basically inviscid mechanisms.[33] However reconnection is crucial in order to allow the separation and migration of pairs of counter-rotating vortex filaments away from the axis of the jet.[36] Thus vortex line element methods are unable to capture the later part of the secondary instability dynamics.

In order to ascertain the ability of NLSE to qualitatively reproduce the postreconnection development of a three-dimensional round jet's secondary instabilities, we have chosen to study a jet defined by Michalke.[37] The velocity profile is

$$U(r)=\frac{U_0}{2}\left[1+\tanh\left(\frac{R(1-r/R)}{2\theta}\right)\right], \tag{73}$$

where U_0 is the centerline velocity on the jet axis x, $r=\sqrt{y^2+z^2}$ is the radial coordinate, θ is the momentum thickness, and R is the jet radius. We have simulated the NLSE in the geometry adapted to the jet as described in Ref. 13 and performed several runs with the following jet parameters: $U_0=1;\theta=0.16;R=1$; and $c=1.25;\xi=0.05/\sqrt{2}$.

The corresponding unperturbed ARGLE converged state, $\psi_{\rm jet}$, is shown in Fig. 21(a) to consist of an array of vortex rings. The converged three-dimensional jet solution $\psi_{\rm jet}$ is then perturbed via

$$\psi(x,r)=\psi_{\rm jet}(x,r)+\epsilon\mathbf{U}\cdot\boldsymbol{\nabla}\psi_{\rm jet}(x,r).$$

An axisymmetric perturbation velocity **U** leads to the primary Kelvin-Helmoltz instability shown in Fig. 21(b). The addition of a small nonaxisymmetric component to **U** as in the viscous computations[36] leads to the states shown in Figs. 21(c) and 22.

These final states display a striking resemblance with the viscous results shown in Ref. 36. Pairs of counter-rotating axial vortices give rise to the outwardly migrating vortex rings shown in Fig. 22 as in the viscous calculations.

Although the results presented in this section are preliminary, they nevertheless strongly support the conjecture of universality of reconnection processes, at least in the case of secondary instabilities of free-shear flows.

V. CONCLUSION

The main result of the NLSE simulations presented in this paper is that two diagnostics of Kolmogorov's regime in decaying turbulence are satisfied. These diagnostics are, at the time of the maximum of energy dissipation; (i) a parameter-independent kinetic energy dissipation rate, and (ii) a $k^{-5/3}$ spectral scaling in the inertial range. Thus, the NLSE simulations were shown to be very similar, as far as energetics is concerned, with the viscous simulations.

Experimentally, towed grid superfluid turbulence has been used in helium II to probe the decay of eddies by monitoring the attenuation of second sound.[17] It was found that the line density of quantum vortices follow the Kolmogorov law $\omega\sim t^{-3/2}$. This result was interpreted by the locking of the normal fluid and the superfluid via mutual friction. An experiment that would correspond to the numerical results of the present article should be performed at a temperature low enough for the normal component of the flow to be ne-

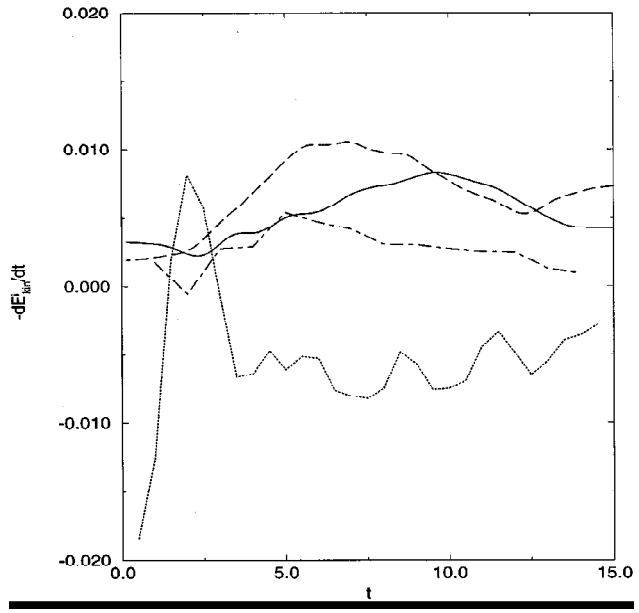

FIG. 20. Incompressible kinetic energy dissipation, $-dE^i_{\rm kin}/dt$, under NLSE dynamics: $c=1$ (dotted); $c=1.5$ (dot-dashed); $c=2$ (solid) and $c=4$ (dashed). All runs are performed with $N=256$ and $\xi=0.1/(4\sqrt{2})$ (see Table III).

glected. In this low temperature regime, second sound attenuation measurements cannot be performed.

In the case of helium, the viscosity at the critical point ($T=5.174$ K, $P=2.2\times10^5$ Pa) is given by $\nu_{\rm cp}=0.27\times10^{-7}$ m^2 s^{-1}. The quantum of circulation, $\Gamma=h/m_{\rm He}$ has the value 0.99×10^{-7} m^2 s^{-1}. Thus, $\nu_{\rm cp}\sim0.25\Gamma$. Using $\Gamma\sim l_0u_0$ and (71), one finds $d_{\rm bump}\sim l_0/\sqrt{R_{\rm cp}}\sim l_\lambda$ where $R_{\rm cp}$ is the integral scale Reynolds number at the critical point and l_λ the Taylor microscale. In other words, the value of $d_{\rm bump}$ in a superfluid helium experiment performed at $T=1$ K is thus of the same order as the Taylor microscale in the same experimental setup run with viscous helium at the critical point.[38]

Preliminary measurement [J. Maurer, (*private communication*)] in the swirling flow of Ref. 23 did not seem to show a significant change in energy dissipation for temperatures as low as 1.6 K, where the normal fluid and the superfluid are in the same proportion. It would be interesting to know if this behavior persists at $T<1$ K. A Kolmogorov regime at such a low temperature was predicted in Ref. 39 based on a simplified model of a self-crossing vortex line.

An open interesting question is to know how far the analogy between superfluid and ordinary turbulence can be pushed. In particular, in the field of viscous turbulence, it is well known that Kolmogorov's theory is only approximate, since it neglects intermittency.[28] Inertial range ''intermittency corrections'' are routinely measured[40,23,41,42] on velocimetry data, by looking at the scaling of high order moments of velocity increments. If the corresponding superfluid quantities could be measured experimentally (this would suppose the existence of a velocimetry probe working below $T=1$ K), significant differences might appear.

Another point is that Kolmogorov's scaling still eludes the derivation from first principles, i.e., from the Navier–Stokes equations.[28] This is a baffling situation, because although approximate, Kolmogorov's scaling is well supported experimentally. There is some hope that NLSE could shed new light on these hard problems.

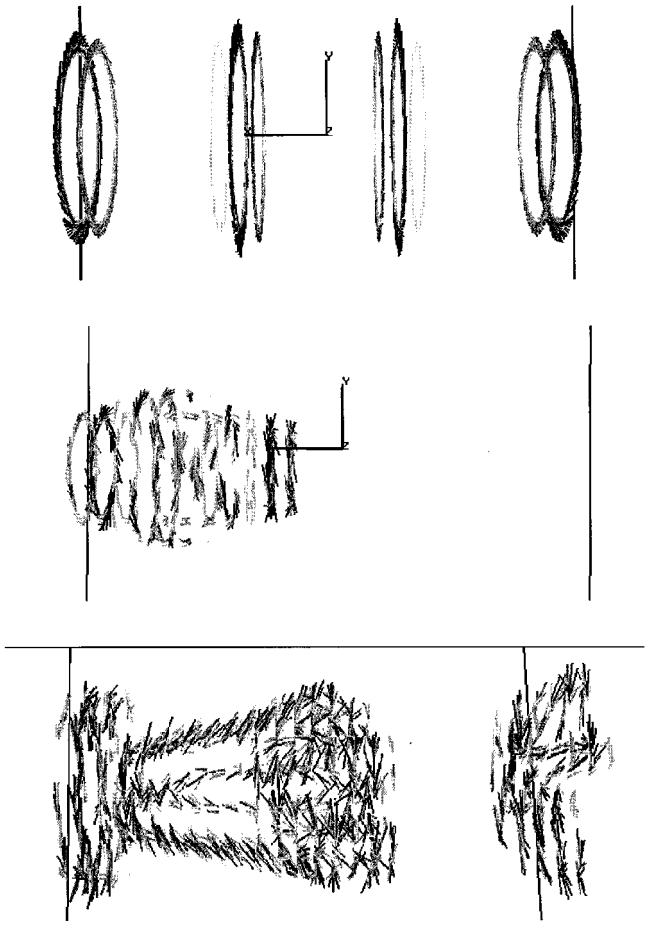

FIG. 21. Three-dimensional visualizations of $\nabla\times(\rho\mathbf{v})$: (a) initial three-dimensional round jet; (b) large ring resulted from the Kelvin-Helmholtz instability; (c) secondary instability. Note the formation of axial contra-rotating vortex filaments.

ACKNOWLEDGMENTS

Computations were performed on the C94–C98 of the Institut du Développement et des Ressources en Informatique Scientifique. We would like to thank L. Tuckerman for her helpful discussions on this work.

APPENDIX: NUMERICAL METHODS

We have chosen to use pseudospectral methods both for their precision and for their ease of implementation.[43] For NLSE, we use the fractional step method described in Ref. 44. Our numerical methods are thus standard; their only specialty stems from the conjunction of the Taylor–Green symmetries with NLSE.

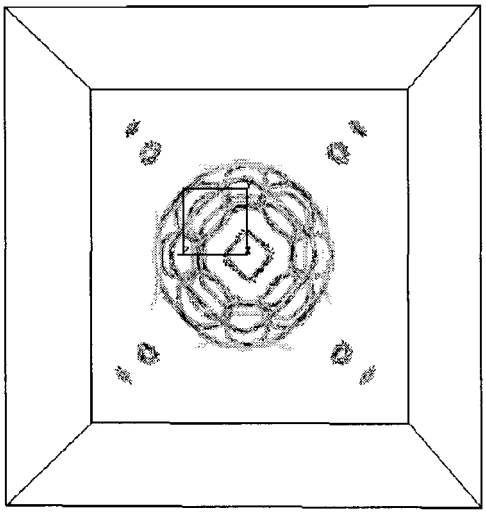

FIG. 22. Reconnection after secondary instability of a three-dimensional round jet: note the formation of radially propagating small rings which correspond to side jets.

1. Taylor–Green spectral representation for NLSE

a. Taylor–Green spectral representation

The symmetries of the TG velocity field (61) implemented in the code are rotational symmetry of angle π around the axis $(x=z=\pi/2)$, $(y=z=\pi/2)$, and $(x=y=\pi/2)$ and mirror symmetry with respect to the planes $x=0,\pi$, $y=0,\pi$, $z=0,\pi$. The advective velocity is parallel to these planes that form the sides of the *impermeable box* which confines the flow. It is demonstrated in Ref. 19 that these symmetries are equivalent to the following Fourier expansions for the velocity field $\mathbf{u}(x,y,z,t)$, solution of the Navier–Stokes equations with initial data $\mathbf{u}^{\mathrm{adv}}$ (61):

$$\begin{aligned} u_x(x,y,z,t) &= \sum_{m=0}^{\infty}\sum_{n=0}^{\infty}\sum_{p=0}^{\infty} \hat{u}_x(m,n,p,t) \\ &\quad \times \sin mx \cos ny \cos pz, \\ u_y(x,y,z,t) &= \sum_{m=0}^{\infty}\sum_{n=0}^{\infty}\sum_{p=0}^{\infty} \hat{u}_y(m,n,p,t) \\ &\quad \times \cos mx \sin ny \cos pz, \\ u_z(x,y,z,t) &= \sum_{m=0}^{\infty}\sum_{n=0}^{\infty}\sum_{p=0}^{\infty} \hat{u}_z(m,n,p,t) \\ &\quad \times \cos mx \cos ny \sin pz \end{aligned} \tag{A1}$$

where $\hat{\mathbf{u}}(m,n,p,t)$ vanishes unless m,n,p are either all even or all odd integers. There exist additional relationships between the expansion coefficients corresponding to the rotational symmetry of angle $\pi/2$ around the axis $(x=y=\pi/2)$:

$$\begin{aligned} \hat{u}_x(m,n,p,t) &= (-1)^{r+1}\hat{u}_y(n,m,p,t), \\ \hat{u}_z(m,n,p,t) &= (-1)^{r+1}\hat{u}_z(n,m,p,t) \end{aligned} \tag{A2}$$

where $r=1$ when m,n,p are all even and $r=2$ when m,n,p are all odd.

It is easy to show that expressions (A1) applied to ρv_j [see Eq. (26)] correspond to the following decomposition for the complex scalar $\psi(x,y,z,t)$, solution of NLSE:

$$\begin{aligned} \psi(x,y,z,t) &= \sum_{m=0}^{\infty}\sum_{n=0}^{\infty}\sum_{p=0}^{\infty} \hat{\psi}(m,n,p,t) \\ &\quad \times \cos mx \cos ny \cos pz, \end{aligned} \tag{A3}$$

with $\hat{\psi}(m,n,p,t)=0$ unless m,n,p are either all even or all odd integers. The additional conditions are then:

$$\hat{\psi}(m,n,p,t) = (-1)^{r+1}\hat{\psi}(n,m,p,t), \tag{A4}$$

with the same convention as above. Implementing these relations yields savings of a factor 64 in computational time and memory size when compared to general Fourier expansions.

b. Taylor–Green Clebsch potentials

The Taylor–Green velocity field (61) has an associated vorticity field

$$\begin{aligned} \omega_x(x,y,z) &= -\cos(x)\sin(y)\sin(z), \\ \omega_y(x,y,z) &= -\sin(x)\cos(y)\sin(z), \\ \omega_z(x,y,z) &= 2\sin(x)\sin(y)\cos(z). \end{aligned} \tag{A5}$$

In order to use our preparation method (see Sec. III C), Clebsch potentials $\lambda(x,y,z)$, and $\mu(x,y,z)$ such that $\boldsymbol{\omega}=\boldsymbol{\nabla}\lambda\times\boldsymbol{\nabla}\mu$ are needed. Thus λ and μ must be invariants under the vorticity field dynamics.

Looking for a general invariant, s, under the vorticity field dynamics, one must solve the equation

$$\omega_j\partial_j s(x,y,z)=0, \tag{A6}$$

which gives, dividing by $\sin(x)\sin(y)\sin(z)$:

$$\frac{\partial_x s}{\tan(x)}+\frac{\partial_y s}{\tan(y)}-2\frac{\partial_z s}{\tan(z)}=0. \tag{A7}$$

This equation is separable: using the substitution $s(x,y,z)=u(x)v(y)w(z)$, and dividing by s, one gets the equation

$$\frac{\partial_x \ln[u(x)]}{\tan(x)}+\frac{\partial_y \ln[v(y)]}{\tan(y)}-2\frac{\partial_z \ln[w(z)]}{\tan(z)}=0. \tag{A8}$$

Thus, each term of (A8) must be equal to a constant, c_x, c_y, and c_z, respectively, satisfying

$$c_x+c_y-2c_z=0. \tag{A9}$$

Each separated equation to be solved is then:

$$\frac{\partial_x \ln[u(x)]}{\tan(x)}=c_x, \tag{A10}$$

whose general solution is given by $u(x)=\mathrm{const}(\cos x)^{-c_x}$. Two independent solutions of (A9) are $c_x=-1,c_y=0,c_z=-1/2$ and $c_x=0,c_y=-1,c_z=-1/2$.

Using these two solutions for s, one can define the Clebsch potentials

$$\begin{aligned} \lambda_1(x,y,z) &= \sqrt{2}\cos(x)\sqrt{\cos(z)}, \\ \mu_1(x,y,z) &= \sqrt{2}\cos(y)\sqrt{\cos(z)}. \end{aligned} \tag{A11}$$

It is easy to check that $\nabla\lambda_1\times\nabla\mu_1$ is equal to (A5). However, these Clebsch potentials are real for $\cos(z)>0$ and purely imaginary for $\cos(z)<0$. In order to be able to apply our preparation method described in Sec. III C, we need real and periodic Clebsch potentials.

One can easily check that, replacing (A11) by

$$\lambda(x,y,z)=\sqrt{2}\,\cos(x)\sqrt{|\cos(z)|},$$
$$\mu(x,y,z)=\sqrt{2}\,\cos(y)\sqrt{|\cos(z)|}\,\mathrm{sgn}(\cos z) \tag{A12}$$

does not change the vorticity field, provided that $\cos(z)\neq 0$. However, the singularity of (λ,μ) on the plane defined by $\cos(z)=0$ due to the derivative of the function sgn is of the form $2\delta[\cos(z)]\sqrt{|\cos(z)|}=0$ and is thus harmless.

c. Compatibility of the Clebsch potentials with the representation

Expanding (λ,μ) defined by (A12) as cosine series:

$$\lambda(x,y,z)=\sum_{m_\lambda=0}^{\infty}\sum_{n_\lambda=0}^{\infty}\sum_{p_\lambda=0}^{\infty}\hat{\lambda}(m_\lambda,n_\lambda,p_\lambda,t)\times\cos m_\lambda x\,\cos n_\lambda y\,\cos p_\lambda z,$$
$$\mu(x,y,z)=\sum_{m_\mu=0}^{\infty}\sum_{n_\mu=0}^{\infty}\sum_{p_\mu=0}^{\infty}\hat{\mu}(m_\mu,n_\mu,p_\mu,t)\times\cos m_\mu x\,\cos n_\mu y\,\cos p_\mu z, \tag{A13}$$

it is easy to check, looking at the parity of (A12) under each of the transformations:

$$\cos x\to-\cos x,$$
$$\cos y\to-\cos y, \tag{A14}$$
$$\cos z\to-\cos z,$$

that the only nonzero terms in (A13) are such that m_λ is odd while n_λ and p_λ are even and m_μ is even while n_μ and p_μ are odd. Then, because of the form of (λ,μ) (A13), to check that a given function of (λ,μ) is odd or even under each of the parity transformations (A14) is equivalent to checking its parity under the substitutions:

$$\lambda\to-\lambda,$$
$$\mu\to\mu, \tag{A15}$$

or,

$$\lambda\to\lambda,$$
$$\mu\to-\mu. \tag{A16}$$

Thus, even powers of λ and μ involve only even wave numbers whereas odd powers of λ μ involve only odd wave numbers.

Writing the real and imaginary parts of ψ_4 (55) in terms of λ and μ, it is straightforward to check that, under the substitutions (A15) and (A16), $\mathrm{Re}\psi_4\to\mathrm{Re}\psi_4$ and $\mathrm{Im}\psi_4\to-\mathrm{Im}\psi_4$. Thus, the initial data ψ_4 has a real part that involves only even wave numbers and an imaginary part that involves only odd wave numbers. Furthermore, ψ_4 obeys the supplementary conditions (A4) because the corresponding rotation amounts to a circular permutation of each of the factors in (55).

The numerical integration, using ARGLE, shows that the final state has a good spectral convergence, in contrast with the Clebsch initial data ψ_4 (see Fig. 12).

2. Time stepping schemes

Two pseudospectral codes were written for integrating ARGLE and NLSE using the expansion (A3). Expressing the evolution equation in the form

$$\frac{\partial\psi}{\partial t}=L\psi+NL(t),$$

where NL stands for the simplest nonlinear term (17) and L for the linear operator, the following time stepping schemes are used.

a. Time stepping for ARGLE

The time stepping for ARGLE is first-order accurate

$$\psi(t+\Delta t)=\frac{\psi(t)+NL(t)\Delta t}{1-L\Delta t}$$

where $L=\alpha\nabla^2$ and $NL=(\Omega-\beta|\psi|^2)\psi$. If a fixed point is reached, it is the correct steady state, independently of the time step.

b. Time stepping for NLSE

We use the fractional steps method described in Ref. 44, with $L=i\alpha\nabla^2$ and $NL=i(\Omega-\beta|\psi|^2)\psi$. In one fractional step, the following linear problem is solved in spectral space:

$$\hat{\psi}_k(t+\Delta t)=\exp(-i\alpha k^2\Delta t)\hat{\psi}_k(t).$$

The result is then transformed to physical space where the second fractional step is solved as:

$$\psi(x,t+\Delta t)=\exp\{i[\Omega-\beta|\psi(x,t)|^2]\Delta t\}\psi(x,t).$$

The two steps are alternated in order to maintain second-order accuracy in time through Strang-type splitting. They conserve the modulus of ψ. The conservation of the total energy E_{tot} [see Eq. (33)] is monitored as an accuracy check.

The ARGLE and NLSE codes were validated by comparison with three-dimensional general pseudospectral codes.[12,13] At a resolution of 512^3 (the maximum used in this article) with a time step $\Delta t=1/6400$, one time unit of NLSE integration requires 7.5 h of CPU time on a Cray 90 machine.

3. Computations of the spectra

a. Computations of the energy spectra of a two-dimensional vortex

The numerical computations of the spectra were performed with Mathematica using the function f defined in (17). We begin to carry on these computations with $\xi=1/\sqrt{2}$, $c=1$, and the density at infinity $\rho_0=1$ and we will recover the dimensional spectra at the end of this section. As $\rho(r)$ explicitly appears into the integrals (41), (42), we first need to compute it numerically. To wit, we use an expansion

in mapped Chebychev polynomials. The mapping is defined by $r=lz/(1-z^2)$ or $z=(2r/l)/(1+\sqrt{1+4(r/l)^2})$, which maps the interval $0\leqslant r<\infty$ into the interval $0\leqslant z\leqslant 1$ and where l is a nonzero parameter controlling the distribution of collocation points. Since $\sqrt{\rho(r)}$ is an odd function of r, the expansion will be over only odd polynomials. Thus $\sqrt{\rho(r)}$ is expanded as

$$\sqrt{\rho(r)}=\sum_{n=0}^{N+1}\widehat{\sqrt{\rho}}_n T_{2n+1}\left(\frac{2r/l}{1+\sqrt{1+4(r/l)^2}}\right), \tag{A17}$$

where $\widehat{\sqrt{\rho}}_N$ and $\widehat{\sqrt{\rho}}_{N+1}$ are fixed to satisfy the boundary conditions

$$\lim_{r\to\infty}\sqrt{\rho(r)}=1,$$

$$\lim_{r\to\infty} r(\sqrt{\rho(r)}-1)=0.$$

The axisymmetric two-dimensional vortex solution is obtained by minimization of the following free energy:

$$\mathscr{F}[\rho]=\int 2\pi r dr\left[\frac{1}{2}\left(\frac{\partial\sqrt{\rho}}{\partial r}\right)^2+\frac{\sqrt{\rho}^2}{2r^2}+\frac{\sqrt{\rho}^4}{2}-\sqrt{\rho}^2+\frac{1}{2}-\frac{r^2}{2(1+r^4)}\right].$$

The ρ independent term in the above expression has been included to cancel the large-r logarithmic divergence of the kinetic energy of the vortex. The minimization is obtained by time integration of the corresponding Euler–Lagrange equation. The expansion (A17) used with $l=2$ converges rapidly. With $N=10$ Chebychev polynomials, this expansion reproduces the numerical values for the vortex profile $\sqrt{\rho(r)}$ given in Ref. 26 with five digit accuracy.

We then need to evaluate numerically integrals involving Bessel function (41). In order to take into account the singularity at $r=\infty$, we cut the integral in two parts:

$$\hat{g}(k)=\frac{1}{(2\pi)}\int_0^{r_{\max}} dr\ r\ g(r)\ J_0(kr)+\frac{1}{(2\pi)}\int_{r_{\max}}^{+\infty} dr\ r\ g(r)\ J_0(kr).$$

The first term is evaluated numerically with the full expressions of g and $J_0(kr)$. In the second term, we replace $J_0(kr)$ by its asymptotic form and $rg(r)$ by fitting to a large-r expansion $\Sigma_{n=2}^{5}\beta_n/r^n$. The approximate formula is thus:

$$\hat{g}(k)\approx\int_0^{r_{\max}} dr\ r\ g(r)\ J_0(kr)+\sum_{n=2}^{5}\int_{r_{\max}}^{+\infty} dr\ r\ \frac{\beta_n}{r^n}\sqrt{\frac{2}{\pi kr}}\cos\left(kr-\frac{\pi}{4}\right).$$

Using dimensional analysis, it is straightforward to show that, with $\rho_0=1$, all the spectra (41), (42) verify

$$\int E_d(k_d)dk_d=c^2(\xi\sqrt{2})^2\int E_m(k_m)dk_m,$$

where E_d and k_d denote the dimensionalized spectra and wave number corresponding to arbitrary values of ξ and c while E_m and k_m denote the spectra and wave number corresponding to $\xi=1/\sqrt{2}$ and $c=1$. Thus the spectra $E_d(k_d)$ are obtained from $E_m(k_m)$ as

$$E_d(k_d)=c^2(\xi\sqrt{2})^3E_m(\xi\sqrt{2}k_d). \tag{A18}$$

b. Computations of the energy spectra in the periodic codes

The energy spectra are computed in the following way: First, we evaluate

$$\frac{2\alpha\overline{\psi}\partial_j\psi}{\sqrt{|\psi|^2+\epsilon^2}}, \tag{A19}$$

where ϵ is a small regularizing parameter. Then, using the relation (26), the real part of (A19) is found to be $2\alpha\partial_j\sqrt{\rho}$ and the imaginary part to be $\sqrt{\rho}v_j$. Furthermore, in order to separate the kinetic energy corresponding to compressibility, we decompose $\sqrt{\rho}v_j$ into $\sqrt{\rho}v_j=(\sqrt{\rho}v_j)^i+(\sqrt{\rho}v_j)^c$ with $\nabla.(\sqrt{\rho}v_j)^i=0$. Using these quantities, we compute the spectra (37) [with the simplest form of f (17)].

The angle-averaged spectra are then evaluated by summing the square modulus of the above quantities in shells in Fourier space. A mode m,n,p belongs to the shell numbered as $[\sqrt{m^2+n^2+p^2}+1/2]$.

The density momentum spectrum $J(k)$ is computed in the same way, by using the imaginary part of $2\alpha\overline{\psi}\partial_j\psi$ and decomposed into a compressible part J^c and an incompressible part J^i.

[1] L. Landau and E. Lifchitz, *Fluid Mechanics* (Pergamon, Oxford, 1980).
[2] K. W. Schwarz, ''Three-dimensional vortex dynamics in superfluid ^{4}He: line-line and line-boundary interactions,'' Phys. Rev. B **31**, 5782 (1985).
[3] E. P. Gross, ''Hydrodynamics of a superfluid condensate,'' J. Math. Phys. (N.Y.) **4**, 195 (1963).
[4] V. L. Ginzburg and L. P. Pitaevskii, ''On the theory of superfluidity,'' Sov. Phys. JETP **34**, 858 (1958).
[5] R. J. Donnelly, *Quantized Vortices in Helium II* (Cambridge University Press, Cambridge, 1991).
[6] A. L. Fetter, ''Vortices in an imperfect bose gas IV. Translational velocity,'' Phys. Rev. **151**, 100 (1966).
[7] J. C. Neu, ''Vortices in complex scalar fields,'' Physica D **43**, 385 (1990).
[8] F. Lund, ''Defect dynamics for the nonlinear Schrödinger equation derived from a variational principle,'' Phys. Rev. Lett. **159**, 245 (1991).
[9] P. Nozières and D. Pines, *The Theory of Quantum Liquids* (Addison Wesley, New York, 1990).
[10] T. Frisch, Y. Pomeau, and S. Rica, ''Transition to dissipation in a model of superflow,'' Phys. Rev. Lett. **69**, 1644 (1992).
[11] Y. Pomeau and S. Rica, ''Model of superflow with rotons,'' Phys. Rev. Lett. **71**, 247 (1993).
[12] C. Nore, M. Brachet, and S. Fauve, ''Numerical study of hydrodynamics using the nonlinear Schrödinger equation,'' Physica D **65**, 154 (1993).
[13] C. Nore, M. Abid, and M. Brachet, ''Simulation numérique d'écoulements cisaillés tridimensionnels à l'aide de l'équation de Schrödinger non linéaire,'' C.R.A.S **319**, 733 (1994).
[14] J. Koplik and H. Levine, ''Vortex reconnection in superfluid helium,'' Phys. Rev. Lett. **71**, 1375 (1993).
[15] C. Nore, M. Brachet, E. Cerda, and E. Tirapegui, ''Scattering of first sound by superfluid vortices,'' Phys. Rev. Lett. **72**, 2593 (1994).
[16] R. P. Feynman, *Application of Quantum Mechanics to Liquid Helium*, Vol. I of *Progress in Low Temp.* (North-Holland, Amsterdam, 1955).
[17] M. Smith, R. Donnelly, N. Goldenfeld, and W. Vinen, ''Decay of vorticity in homogeneous turbulence,'' Phys. Rev. Lett. **71**, 2583 (1993).
[18] G. I. Taylor and A. E. Green, ''Mechanism of the production of small

eddies from large ones,'' Proc. R. Soc. London, Ser. A **158**, 499 (1937).
[19]M. E. Brachet, D. I. Meiron, S. A. Orszag, B. G. Nickel, R. H. Morf, and U. Frisch, ''Small-scale structure of the Taylor-Green vortex,'' J. Fluid Mech. **130**, 411 (1983).
[20]M. Brachet, ''Géométrie des structures à petite échelle dans le vortex de Taylor-Green, C.R.A.S II **311**, 775 (1990).
[21]J. Domaradzki, W. Liu, and M. Brachet, ''An analysis of sugrid-scale interactions in numerically simulated isotropic turbulence,'' Phys. Fluids A **5**, 1747 (1993).
[22]S. Douady, Y. Couder, and M. E. Brachet, ''Direct observation of the intermittency of intense vorticity filaments in turbulence,'' Phys. Rev. Lett. **67**, 983 (1991).
[23]G. Zocchi, P. Tabeling, J. Maurer, and H. Willaime, ''Measurement of the scaling of the dissipation at high Reynolds numbers,'' Phys. Rev. Lett. **50**, 3693 (1994).
[24]S. Fauve, C. Laroche, and B. Castaing, ''Pressure fluctuations in swirling turbulent flows,'' J. Phys. (France) II **3**, 271 (1993).
[25]E. A. Spiegel, ''Fluid dynamical form of the linear and nonlinear Schrödinger equations,'' Physica D **1**, 236 (1980).
[26]M. P. Kawatra and R. K. Pathria, ''Quantized vortices in imperfect Bose gas,'' Phys. Rev. **151**, 1 (1966).
[27]H. Goldstein, *Classical Mechanics*, Addison-Wesley Series in Physics (Addison-Wesley, Reading, MA, 1980).
[28]U. Frisch, *Turbulence, the Legacy of A. N. Kolmogorov* (Cambridge University Press, Cambridge, 1995).
[29]H. Lamb, *Hydrodynamics* (Cambridge University Press, Cambridge, 1963).
[30]V. Arnold, *Mathematical Methods of Classical Mechanics* (Springer-Verlag, New York, 1978), Vol. 60.
[31]M. Brachet, M. Meneguzzi, A. Vincent, H. Politano, and P. L. Sulem, ''Numerical evidence of smooth self-similar dynamics and possibility of subsequent collapse for three-dimensional ideal flows,'' Phys. Fluids A **4**, 2845 (1992).
[32]A. J. Chorin, ''Numerical study of slightly viscous flow,'' J. Fluid Mech. **57**, 785 (1973).
[33]E. Meiburg, J. C. Lasheras, and J. E. Martin, ''Experimental and numerical analysis of the three-dimensional evolution of an axisymmetric jet,'' *Turbulent Shear Flows* **7**, 195 (1991).
[34]T. Passot and A. Pouquet, ''Numerical simulation of compressible homogeneous flows in the turbulent regime,'' J. Fluid Mech. **181**, 441 (1987).
[35]D. Liepmann and M. Gharib, ''The role of streamwise vorticity in the near-field entrainment of round jets,'' J. Fluid Mech. **245**, 643 (1992).
[36]M. Abid and M. Brachet, ''Numerical characterization of the dynamics of vortex filaments in round jets,'' Phys. Fluids A **5**, 2582 (1993).
[37]A. Michalke, ''On the inviscid instability of the hyperbolic-tangent velocity profile,'' J. Fluid Mech. **19**, 543 (1964).
[38]C. Nore, M. Abid, and M. E. Brachet, ''Kolmogorov turbulence in low-temperature superflows, Phys. Rev. Lett. **78**, 3896 (1997).
[39]B. V. Svistunov, ''Superfluid turbulence in the low-temperature limit,'' Phys. Rev. B **52**, 3647 (1995).
[40]Y. Gagne, E. Hopfinger, and U. Frisch, ''A new universal scaling for fully developed turbulence: The distribution of velocity increments,'' NATO ASI **237**, 315 (1990).
[41]F. Belin, P. Tabeling, and H. Willaime, ''Exponents of the structure functions in a low temperature helium experiment, '' Physica D **93**, 52 (1996).
[42]A. Arneodo *et al.* ''Structure functions in turbulence, in various flow configurations, at Reynolds number between 30 and 5000, using extended self-similarity,'' Europhys. Lett. **34**, 411 (1996).
[43]D. Gottlieb and S. A. Orszag, *Numerical Analysis of Spectral Methods* (SIAM, Philadelphia, 1977).
[44]R. Klein and A. J. Majda, ''Self-stretching of perturbed vortex filaments,'' Physica D **53**, 267 (1991).